REVIEW

Check for updates

Characterization of organic light-emitting diodes using impedance spectroscopy and equivalent circuits

Akeem Raji, [ID] Jaeyong Park, Jonghee Lee [ID] and Jae-Hyun Lee [ID] *

Operational mechanisms in organic light-emitting diodes (OLEDs) based on single molecules or conjugated polymers, under different conditions, have been extensively investigated using a variety of techniques. This review discusses the studies from pioneering groups that advanced the use of impedance spectroscopy (IS) and equivalent circuit techniques to investigate these mechanisms in OLEDs. Emphasis is placed on foundational and contemporary studies that have advanced the use of IS and equivalent circuit simulation techniques to analyze charge transport, accumulation, and interfacial dynamics within OLED structures. The theoretical basis of IS as a transfer function, along with the principles of equivalent circuit simulation, is discussed in detail. Special attention is given to the application of these techniques in identifying trap states and assessing device degradation. Additionally, this review examines alternative representations and complementary measurements used in conjunction with IS for probing OLED behavior. Collectively, the findings underscore IS and equivalent circuit simulation as robust analytical methods, offering critical insights into the performance and stability of organic electronic devices.

1. Introduction

Prior to the invention and optimization of organic light-emitting diode (OLED) devices, displays originated from cathode ray tubes (CRTs) and then transitioned to liquid-crystal displays (LCDs).[1] Since the invention of the first OLED display by Slyke and Tang,[2,3] simplifying the device structure and improving its efficiency and stability has been at the center of research for many research institutes and personnel. By doing so, one of the major improvements was the migration from the first invented fluorescent OLED device[2,3] to phosphorescent (PH)[4–7] and currently to thermally activated delayed fluorescent (TADF) OLED devices.[8–10] Future research is looking to migrate to hyperfluorescent OLED devices.[11,12] These names are assigned to the devices based on their respective emission mechanisms in the emission layer (EML). Another important

Department of Creative Convergence Engineering, Hanbat National University, Daejeon, 34158, South Korea. E-mail: jhyunlee@hanbat.ac.kr; Tel: +82-42-821-1970

Akeem Raji received his BSc degree in Materials Engineering from Kwame Nkrumah University of Science and Technology, Kumasi, Ghana, in 2018. He proceeded to further his education in South Korea, where he obtained his Master of Engineering degree (MEng) from Hanbat National University. He is currently a PhD student at the same University. His research is focused on organic semiconductors and nanofabrication of thin films.

Akeem Raji

Jae-Yong Park received her BS degree from Hanbat National University, South Korea, in 2024. He is currently taking the MS course at the Department of Creative Convergence Engineering at the same University. His research interests include impedance analysis.

Jaeyong Park

improvement is the electrical optimization of OLEDs using newly synthesized molecules with optimized highest occupied molecular orbital (HOMO) or lowest unoccupied molecular orbital (LUMO) energy levels, high charge mobility, and electrical doping efficiencies. Presently, organic molecules with inherent permanent dipole moments (PDMs) that create what is known as spontaneous orientation polarization (SOP) during thermal vaporization have also been used to improve the performance of OLED devices *via* charge injection and charge transport mechanisms.[13,14]

Improving the performance of existing OLED device structures and their electrical characteristics must be accompanied by device assessment to understand the current improving factors and impediment contributing factors that deteriorate the ability of the device to function at its maximum.[15–17] Over the years, different types of assessments/investigating tools/techniques, both destructive and nondestructive, have been developed to investigate the operational mechanisms, including charge injection, charge transport, and charge accumulation at the interfaces, charge trapping, recombination, degradation, exciplex formation, and singlet and triplet formation, to generate and emit light in single- or multilayered OLED devices. To mention a few, transient electroluminescence (TrEL) was developed to investigate charge injection, transport, and trapping in the EML,[18,19] time-of-flight (ToF) to investigate the charge carrier mobility of small molecules,[20,21] magneto-electroluminescence (MEL) to investigate intersystem crossing and reverse intersystem crossing mechanisms between singlet and triplet molecules,[22–31] impedance spectroscopy (IS) to investigate charge accumulation, transport, and trapping mechanisms in OLED devices,[32–34] current density–voltage (*J*–*V*) measurement to investigate charge injection, amount of charges present in the device, and leakage current,[35] and capacitance–voltage (*C*–*V*) measurement to investigate charge accumulation, trapping, and recombination in OLED devices[36] *etc.* as shown in Fig. 1. Among these investigation tools, IS was one of the earliest, nondestructive, and commonly used tools to investigate the operational mechanisms in OLEDs, and is the focus of this review.

IS offers kinetic data for various electrochemical systems and is widely used in studies that are not limited to chemical sensing, energy conversion, semiconductor science, corrosion studies, and storage technologies. For instance, Nijhuis *et al.*[38] investigated the junctions of molecular particles using IS, and Ahmadu *et al.*[39] investigated the electrical and dielectric properties of a chemical compound to ascertain its suitability as a battery electrolyte using the impedance technique. This technique is based on the perturbation of an electrochemical system in equilibrium *via* the application of a sinusoidal signal (alternating current (AC) voltage or AC current) over a wide range of frequencies and monitoring the sinusoidal response (current and voltage, respectively, from the AC signals) of the system toward the applied perturbation.[40] The ability to model both the output and input signals *via* a transfer function over a wide range of frequencies makes IS a reliable technique. This is discussed later in the IS and equivalent circuit sections. The importance of IS as a technique can be attributed to its ability to incisively provide information for various electrical processes such as charging/discharging at the device interfaces, diffusion phenomena, charge transfer reactions *etc.*, although these processes exhibit different time constants (τ) in an OLED device (eqn (1)).

$$\tau = RC \qquad (1)$$

where R is the resistance in ohms, and C is the capacitance in farads (F).

Intuitively, the IS measurement data of an OLED device can be simulated by an equivalent circuit that consists of common passive elements, such as resistors, capacitors, inductors, and sometimes other complicated elements referred to as distributed elements (*e.g.*, constant-phase elements (CPE)) connected

Jonghee Lee

Jonghee Lee received his BS, MS, and PhD in Chemistry from the Korea Advanced Institute of Science and Technology (KAIST), Rep. of Korea, in 2002, 2004, and 2007, respectively. He joined Electronics Telecommunications Research Institute (ETRI), Rep. of Korea, in 2007. Then, he moved to the Institut für Angewandte Photophysik (IAPP) at the Technische Universität Dresden in Germany as a post-doc researcher under an Alexander von Humboldt fellowship in 2010. After 2 years, he joined ETRI again in 2012 and has worked on solution processes as well as light-extraction techniques for organic light-emitting diodes (OLEDs). He has been an associate professor at Hanbat National University, Daejeon, South Korea since 2018.

Jae-Hyun Lee

Jae-Hyun Lee is a professor in the Department of Creative Convergence Engineering at Hanbat National University. He received the BS and PhD degree from the Department of Materials Science and Engineering at Korea University in 2002 and Seoul National University in 2011, respectively. Then he worked as a post-doctoral fellow in Institut für Angewandte Photophysik (IAPP) at Technische Universität Dresden (TU Dresden). His research areas include flexible organic electronics and electrically doped organic semiconductors.
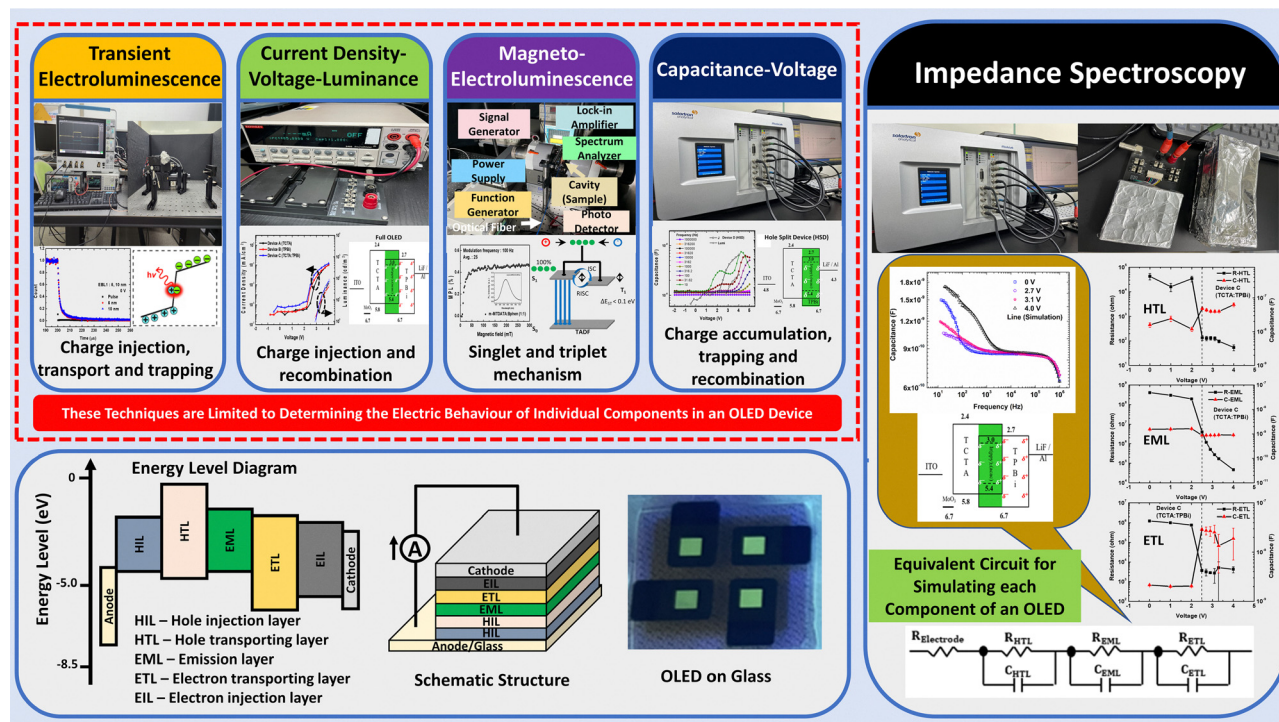
Fig. 1 Some spectroscopic techniques for investigating OLED devices. Reproduced with permission from ref. 37 Copyright 2023, Elsevier Ltd.

to each other in different ways.[41] In this regard, the IS, along with the equivalent circuit simulation of an experimental result, is essential for recognizing the electrical behavior of the individual components in an OLED device. To date, this technique has been applied to OLED devices to better understand numerous electrical parameters using a corresponding circuit model. This has inspired most electrochemical analyzers to develop suitable software that enables the simulation of impedance measurement data using modeled equivalent circuits.

Practically, the frequency range of a measurable OLED device is dictated by the limitations associated with the available instrumentation, connection terminals of the device with an instrument (high-frequency limit), and stability of the device over time (low-frequency limit). It is worth noting that this frequency range, which mostly spans from 10^{-3} Hz to 100 MHz, depending on the equipment, is not calculated, but rather selected in an experimental logic. These unique capabilities have established IS and equivalent circuits as a powerful and highly competitive technique for studies that have significantly intrigued researchers in determining electrical parameters such as contact resistance, bulk resistance and capacitance, time constant (charging/discharging), and other electrical characterizations of OLED devices.

In this review, we discuss works from pioneering groups that used IS and equivalent circuits to characterize OLED devices, purposefully recognizing the electrical behavior of individual components and providing a cogent understanding of numerous electrical parameters within the devices. This paper is organized into sections to first provide a brief tutorial on IS and equivalent circuit simulation and subsequently discuss the pioneering

works conducted to investigate charge accumulation and transport, charge trapping/detrapping, and degradation in OLED devices. The last section presents other commonly used IS techniques in addition to equivalent circuit simulations for investigating OLED devices. Inevitably, understanding the theoretical concepts of IS and equivalent circuits requires minimal mathematical knowledge; however, full comprehension of this technique requires vast information that cannot be solely presented in the tutorial and discussion sections. Therefore, we suggest further reading IS textbooks,[42–45] other tutorials and review articles,[40,41,46] and published papers.[47,48] The next section provides a brief tutorial on IS to help the reader understand and appreciate the basic knowledge complementary to IS and equivalent circuit theory, as well as its analysis.

2. Impedance spectroscopy (IS) and equivalent circuit

2.1. Impedance transfer function

An electrical system, such as OLEDs and other organic electronics, can be investigated by applying an input signal, $x(t)$, to produce an output signal, $y(t)$. Assuming that the system is linear and remains constant with time the input-to-output relationships of the linear time-invariant (LTI) system can be modeled by a transfer function (H) such that $y(t) = H\,[x(t)]$, as illustrated in Fig. 2. Although OLEDs are inherently nonlinear devices, IS can still be applied by operating in the small perturbation regime, where the system's behaviour can be approximated as a linear system.[41] This linearization allows
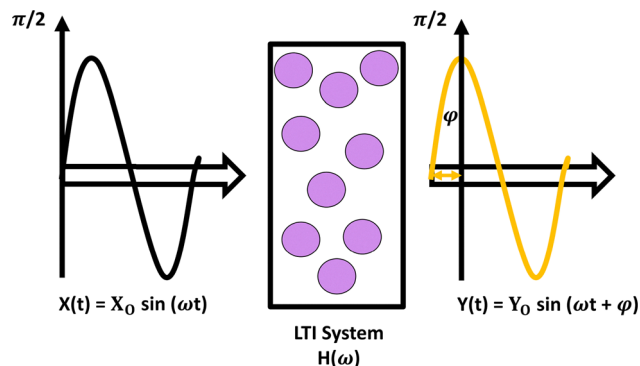
Fig. 2 A schematic diagram representing a linear time-invariant (LTI) system of a transfer function relating an input signal $x(t)$ at a frequency (ω) with the output signal $y(t)$ at the same frequency.

the use of the impedance transfer function to analyze the system's response. If the input signal $x(t)$ is sinusoidal, the output signal $y(t)$ will also be sinusoidal with the same frequency, shifted by an angle φ with respect to the input signal, which is taken as a reference. The transfer function of the LTI system, in the frequency domain, can be expressed as eqn (2):

$$H(\omega) = \frac{\tilde{Y}(\omega)}{\tilde{X}(\omega)} = \frac{X_0}{Y_0} e^{j\varphi} = |H|(\cos\varphi + j\sin\varphi) = H' + jH'' \quad (2)$$

Even though the input and output signals are in the time domain, the transfer function ($H(\omega)$) is a function of frequency and does not depend on either the time or amplitude of the input signal.[40] The transfer function discussed in this review is the impedance of the OLED devices.

Impedance represents the total opposition to the current flow in an electric circuit composed of resistors (R), capacitors (C), and inductors (L). Assuming a low amplitude alternating voltage of a particular frequency in eqn (3) is applied to an OLED device and the resulting alternating current at the same frequency is measured using eqn (4), then the impedance of the device at the same frequency $Z(\omega)$ (transfer function) using eqn (5) based on eqn (2) can be expressed as:

$$V(t) = V_0 \sin(\omega t) \quad (3)$$

$$I(t) = I_0 \sin(\omega t + \varphi) \quad (4)$$

$$Z(\omega) = |Z|e^{j\varphi} = |Z|(\cos\varphi + j\sin\varphi) = Z' + jZ'' \quad (5)$$

where Z is the impedance, Z' is the real part representing the resistance on the x-axis, and Z'' is the imaginary part representing the reactance (opposing AC current flow by capacitance or inductance) on the y-axis.

2.2. Simulation of impedance data with modeled equivalent circuits

The electrical current passing through a pure resistor is always in phase with the applied voltage. In this case, the impedance of the pure resistor is frequency-independent and has only one real impedance component (*i.e.*, resistance). This indicates that the impedance of the pure resistor is $Z = R$ and its phase angle

$(\varphi) = 0°$. However, for a pure capacitor, as an imaginary impedance component, the current passing through it is phase-shifted by 90° in response to the phase of the AC voltage signal. The capacitance of the electrical system, which is characterized by the capacitive reactance (X_c) in eqn 6, decreases with increasing frequency.[41]

$$C = \frac{1}{j\omega X_c} \quad (6)$$

As previously mentioned, IS simulation with an equivalent circuit is a unique technique for retrieving the numerical values of the components in an OLED device included in a modeled circuit. Experimentally measured impedance spectra can be plotted in different formats; however, the two most widely used formats are the Nyquist plot, commonly known as the Cole–Cole plot, and the Bode plot, consisting of capacitance–frequency (C–F) and resistance–frequency (R–F) graphs. These graphs were simulated using modeled equivalent circuits depicting the components of the OLED device. Fig. 3 shows a typical equivalent circuit diagram using a resistor and capacitor in parallel (one RC unit circuit). When the circuit contains a series resistance (R_s) (attributed to the contact resistance which is later discussed) in series connection with a resistor and a capacitor connected in series, the total impedance is expressed as eqn (7):

$$Z(\omega) = R_s + R_{\text{Layer}} + \frac{1}{j\omega C_{\text{Layer}}} \quad (7)$$

where the real part is $Z' = R_{\text{Layer}}$ and the imaginary part $Z'' = 1/\omega C_{\text{Layer}}$.

However, when a series resistor is connected in series with a resistor and a capacitor connected in parallel just as in Fig. 3, the total impedance is expressed as eqn (8):

$$Z(\omega) = R_s + \frac{R_{\text{Layer}}}{1 + (\omega R_{\text{Layer}} C_{\text{Layer}})^2} - j\frac{\omega R_{\text{Layer}}^2 C_{\text{Layer}}}{1 + (\omega R_{\text{Layer}} C_{\text{Layer}})^2} \quad (8)$$

Equivalent circuits of an organic layer are mostly modeled in parallel formats because charges injected into the layer experience a concurrent impedance from the resistance and reactance (capacitance or inductance) of the organic layer in the same time domain, which is different from a series connection of resistance and reactance elements, indicating that the RC components of the organic layer create charge impedance in different time domains. When the components in an OLED
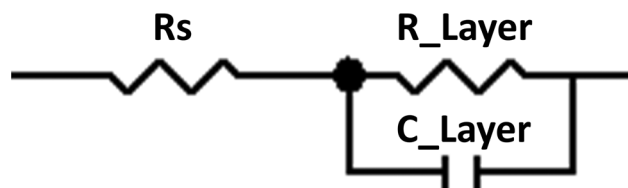

Fig. 3 A typical representation of a parallel connected one RC unit circuit in a series connection with resistance (R_s).

Table 1 Different cases representing the typical behavior of an OLED device with different resistance and capacitance, but constant series resistance

Cases	R_s	R_{Layer} (Ω)	C_{Layer} (nF)
1	50	5000	2.0
2	50	20 000	2.0
3	50	20 000	8.0
4	50	20 000	20.0

device are not fully capacitive, the ideal capacitance (C) in the modeled circuit is supplanted by a CPE. The value of CPE (CPE-P) must be less than one to satisfy its substitution for the ideal capacitance in the circuit, indicating a partially capacitive component. CPEs can also be used to represent surface (lateral) or normal (through the film) distributed time-constant behavior of a film in an OLED device.[49] This method can accurately estimate the effective capacitance and film thickness through the use of the right empirical formula, which depends on the distributed time-constant behavior of the film. Moreover, depending on the device's voltage-dependent diffusion or depletion layer characteristics, CPEs are sometimes employed to represent these behaviors in the device.[50] These common applications of CPE, notwithstanding its reflectance on the surface heterogeneity, roughness, distribution of time constant *etc.* of an organic layer, play a vital role in circuit design and simulation.[51] In this regard, the extracted parameter values (R, C, or CPE) used in the modeled equivalent circuit simulation can be used to investigate mechanisms such as charge transport and accumulation, charge trapping/detrapping, and degradation in OLED devices. It is worth noting that the simulation of an impedance spectrum with an appropriate equivalent circuit requires a deep knowledge of the characteristics of OLED devices.

To demonstrate this, Table 1 lists the resistance and capacitance values for different cases, representing the characteristics of a single-layer OLED device structure with different

resistances and capacitances. The corresponding impedance simulation plots using the Zview software in different formats are presented in Fig. 4 (using a single RC unit), demonstrating the behavior of a typical organic layer with different resistances. A practical simulation of experimental data of device structures with parameters of modeled equivalent circuits at different voltages are provided in Table 2 (in section 5). This presents examples of the use of IS and equivalent circuit to simulate experimentally measured data.

Typical simulated impedance data are from the capacitance–frequency (C–F) simulation. This type of simulation using equivalent circuits has been extensively explored to understand the aforementioned operational mechanisms (charge injection, charge transport, and charge accumulation at the interfaces, charge trapping, recombination, degradation, exciplex formation *etc.*).[52] It is executed by modeling equivalent circuits that physically represent the organic layers within the OLED device, which are then used to simulate the measured C–F curve, as previously mentioned. This is referred to as the fitting process. It is worth noting that the modeled equivalent circuits do not often include passive elements for the hole- and electron-injecting layers (hole injection layer (HIL) and electron injection later (EIL), respectively) owing to their relatively low energy barrier levels (mostly matching the energy level of the electrodes) and relatively small thicknesses. Hence, they are often assumed to be part of their respective electrodes. This technique has generated various C–F interpretations and extracted resistance and capacitance (RC) values depending on the device structure under investigation. Recently, Kim *et al.*[53] adopted this technique to probe the impact of interface mixing on the charge carrier dynamics of a solution-processed OLED device, where the group reported that the diffusion of 2,2′2″-(1,3,5-benzinetriyl)-tris(1-phenyl-1-*H*-benzimidazole) TPBi with a lower glass transition temperature T_g into the EML with a higher T_g promoted nonradiative trap-assisted recombination, resulting in the
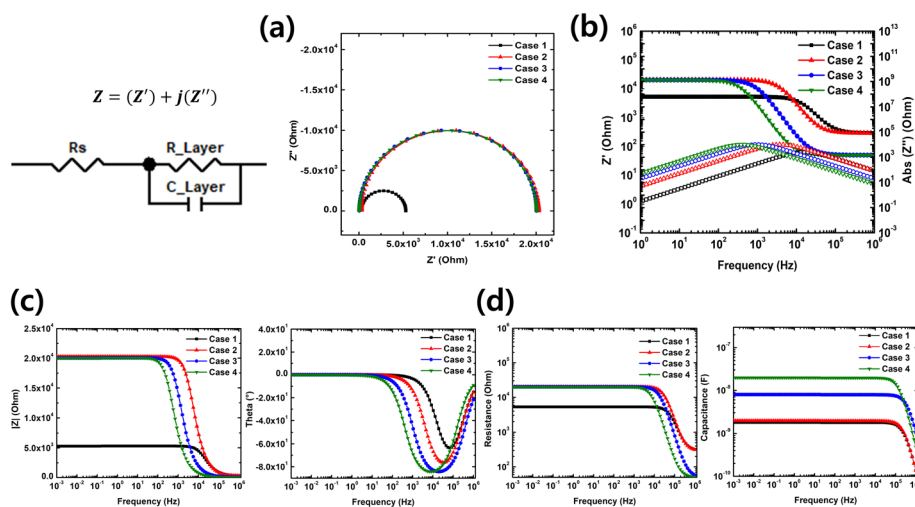
Fig. 4 The simulation results from Zview software using the one RC unit circuit and the values from Table 1 are presented in different impedance spectra. (a) Nyquist (Cole–Cole) plot. (b) Impedance–frequency (Z–F) dependent plot. (c) Absolute impedance–frequency (|Z|–F) and phase (φ)–frequency-dependent plots. (d) The Bode plot constituting: resistance–frequency (R–F) and capacitance–frequency (C–F) plots.

Table 2 Equivalent circuit parameters reported for different structures and modeling circuits

Extracted parameters from equivalent circuit fitting temperature (K)

Structure	Voltage (V)	R_s (Ω)	$R_{b(bulk)}$ (Ω)	$C_{b(bulk)}$ (nF)	$C_{b,trap}$ (nF)	$CPE_{b,trap}$ (Q_b/α_b)	$R_{j(depletion\ junction)}$ (Ω)	$C_{j(depletion\ junction)}$ (nF)	$C_{j,trap}$ (nF)	$CPE_{j,trap}$ (Q_j/α_j)	Active area (cm²)	Temperature (K)	Source
ITO/m-MTDATA/Ag	1.00	175.40	3.65×10^6	0.24	—	—	—	—	—	—	0.01	—	Ref. 72
	1.25	175.30	1.83×10^6	0.24	—	—	—	—	—	—			
	1.50	175.90	8.03×10^5	0.24	—	—	—	—	—	—			
	2.00	177.20	3.78×10^5	0.24	—	—	—	—	—	—			
ITO/m-MTDATA:F$_4$-TCNQ/Ag	0.25	152.20	1781.00	0.09	0.59	7.55×10^4/0.99	5.44×10^4	0.53	2.85	9.63×10^4/0.30			
	0.50	154.70	1502.00	0.77	0.77	7.43×10^4/0.89	1.69×10^4	0.47	2.05	8.68×10^4/0.27			
	0.75	158.80	1196.00	0.10	0.94	7.39×10^4/0.86	5265	0.42	1.52	8.36×10^4/0.23			

Extracted parameters from equivalent circuit fitting temperature (K)

Structure	Voltage (V)	R_s (Ω)	R_{HTL} (Ω)	C_{HTL} (nF)	R_{ETL} (Ω)	C_{ETL} (nF)	$R_{HTL(leakage\ current\ path)}$ (Ω)	$C_{HTL(leakage\ current\ path)}$ (nF)	$R_{ETL(leakage\ current\ path)}$ (Ω)	$C_{ETL(leakage\ current\ path)}$ (nF)	Active area (cm²)	Temperature (K)	Source
ITO/HIL/NPB (50 nm)/Alq$_3$ (40 nm)/LiF/Al	0.00	100.00	1.00×10^9	2.32	1.00×10^9	2.90	1.00×10^9	4.05	1.00×10^9	5.08	0.04	—	Ref. 75
	2.00	760.00		2.32	1.00×10^9	2.90	1.00×10^9	4.06	1.00×10^9	5.08			

Extracted parameters from equivalent circuit fitting temperature (K)

Structure	Voltage (V)	R_s (Ω)	R_{TCTA} (Ω)	C_{TCTA} (nF)	R_{EML} (Ω)	C_{EML} (nF)	R_{TPBi} (Ω)	C_{TPBi} (nF)	$R_{hole\ trap,EML}$ (Ω)	$C_{hole\ trap,EML}$ (nF)	$R_{electron\ trap,EML}$ (Ω)	$C_{electron\ trap,EML}$ (nF)	Active area (cm²)	Temperature (K)	Source
ITO/MoO$_3$ (4 nm)/TCTA (50 nm)/TCTA + TPBi:Ir(p-py)$_2$(acac) (15 nm)/TPBi (50 nm)/LiF/Al	0.00	108.00	42739.00	15.86	4.10×10^8	1.55	1.23×10^6	2.13	—	—	—	—	0.062	—	Ref. 37
	1.00	108.00	16000.00	24.21	3.00×10^8	1.58	1.00×10^6	2.00	—	—	—	—			
	2.00	95.00	34207.00	11.87	1.94×10^8	1.64	759540.00	2.03	—	—	—	—			
	2.50	95.00	134.10	48.81	4.02×10^6	0.88	3693.00	29.06	4.32×10^6	0.45	3.01×10^7	0.13			
	2.70	95.00	127.30	43.84	1.17×10^6	0.88	3133.00	27.49	6.65×10^6	0.11	6.09×10^7	0.07			
	2.90	95.00	130.10	40.12	505040.00	0.89	2831.00	27.01	8.12×10^6	0.10	6.27×10^7	0.08			
	3.10	95.00	125.30	39.90	272150.00	0.89	2719.00	25.37	4.24×10^6	0.18	3.93×10^7	0.19			
	3.30	95.00	96.32	39.80	169190.00	0.91	5084.00	13.45	1.64×10^6	0.41	1.80×10^7	0.23			
	4.00	109.00	54.27	62.89	46276.00	0.91	4252.00	18.91	421650.00	0.65	6.46×10^6	0.35			

Extracted parameters from equivalent circuit fitting temperature (K)

Structure	Voltage (V)	R_s (Ω)	R_{bulk} (Ω)	C_{bulk} (nF)	Z_{trap} (Ω)	Active area (cm²)	Temperature (K)	Source
ITO/p-MeO-TPD/ZnPc:C$_{60}$ (70 nm)/n-C$_{60}$/Al	0.00	40.00	998×10^3	3.83	—	0.064	—	Ref. 78
ITO/p-MeO-TPD/ZnPc:C$_{60}$ (100 nm)/n-C$_{60}$/Al			4.29×10^6	2.68	—			

Extracted parameters from equivalent circuit fitting temperature (K)

Structure	Voltage (V)	R_s (Ω)	R_{bulk} (Ω)	C_{bulk} (nF)	R_{traps} (Ω)	C_{traps} (nF)	Active area (cm²)	Temperature (K)	Source
ITO/p-MeO-TPD/ZnPC:C$_{60}$ (48 nm)/n-C$_{60}$/Al	−1.00	61.00	204.34×10^3	4.73	71.77×10^3	1.97	0.064	—	Ref. 80
	−0.50	61.00	217.59×10^3	4.75	73.02×10^3	2.02			
	0.00	61.00	227.21×10^3	4.79	73.85×10^3	2.11			

Table 2 (continued)

Structure	Voltage (V)	R_s (Ω)	$R_{TPBi:Rb_2CO_3 + NPB:MoO_3}$ (Ω)	$C_{TPBi:Rb_2CO_3 + NPB:MoO_3}$ (nF)	$R_{TPBi + NPB}$ (Ω)	$C_{TPBi + NPB}$ (nF)	$R_{depleted}$ (Ω)	$C_{depleted}$ (nF)	Active area (cm²)	Temperature (K)	Source
ITO/TPBi (70 nm)/TPBi:Rb₂CO₃ (70 nm)/NPB:MoO₃ (70 nm)/NPB (70 nm)/Al (pristine device)	−5.00	80.00	76739.00	8.52	1.49×10^8	1.06	—	—			Ref. 88
	−2.00	81.00	71737.00	8.51	1.57×10^8	1.08	—	—			
	0.00	81.00	76260.00	8.23	1.24×10^8	1.07	—	—			
	2.00	81.00	74540.00	5.22	7.02×10^7	1.17	—	—			
	5.00	80.00	72486.00	4.40	1.09×10^6	1.45	2.99×10^6	7.21			
	8.00	80.00	9605.00	3.08	48580.00	1.73	59976.00	6.31			
ITO/TPBi (70 nm)/TPBi:Rb₂CO₃ (70 nm)/NPB:MoO₃ (70 nm)/NPB (70 nm)/Al (aged device)	−8.00	96.00	398160.00	4.13	1.05×10^8	0.95	—	—			
	−5.00	95.00	233070.00	4.23	1.43×10^8	0.93	—	—			
		95.00									
	−2.00	96.00	312590.00	4.34	1.16×10^8	0.94	—	—			
	0.00	98.00	338340.00	4.40	1.13×10^8	0.92	—	—			
	2.00	99.00	506170.00	4.30	1.54×10^8	0.93	—	—			
	5.00	98.00	490000.00	2.87	1.45×10^7	1.33	1.21×10^7	5.11			
	8.00	97.00	1.65×10^6	1.43	7.13×10^6	2.85	3.57×10^6	4.15			

Extracted parameters from equivalent circuit fitting temperature (K)

Structure	Voltage (V)	R_s (Ω)	$R_{doped NPB}$ (Ω)	$C_{doped NPB}$ (nF)	$R_{intrinsic NPB}$ (Ω)	$CPE_{intrinsic NPB}$ (nF)	Active area (cm²)	Temperature (K)	Source
ITO/NPB:MoO₃ (65 nm)/NPB (5 nm)/Al	—	35.00	10.00×10^4	2.00	1.00×10^6	10.00	0.062	363	Ref. 92
			10.00×10^4		1.50×10^5			373	
			100.00		—	—		383	
ITO/TCTA:MoO₃ (65 nm)/NPB (5 nm)/Al	—	35.00	40.00	20.00	3.00×10^6	10.00	0.062	383	
					10.00×10^6			393	
					10.00×10^6			403	
					27.00×10^6			413	
					27.00×10^6			423	
					8.60×10^3			433	

Extracted parameters from equivalent circuit fitting temperature (K)

Structure	Voltage (V)	R_s (Ω)	R_1 (Ω)	C_1 (nF)	Active area (cm²)	Temperature (K)	Source
ITO/PEDOT:PSSS/SP3/Ca/Al	1.00	—	635.20	7.30	0.09	300	Ref. 102
ITO/PEDOT:PSSS/TP2/Ca/Al			753.50	5.40			

Extracted parameters from equivalent circuit fitting temperature (K)

Structure	Voltage (V)	R_s (Ω)	C_{geo} (nF)	$R_{high conduction bulk}$ (Ω)	$C_{high conduction bulk}$ (nF)	$R_{low conduction bulk}$ (Ω)	$C_{low conduction bulk}$ (nF)	Active area (cm²)	Temperature (K)	Source
ITO/PPV/Al	0.00	73.00	0.76	3.63×10^6	2.58	2.08×10^9	3.63	0.25	186	Ref. 105
		70.00	0.77	3.42×10^5	2.43	2.99×10^7	5.25		206	
		68.00	0.78	5.25×10^4	2.20	5.37×10^6	4.76		222	
		69.00	0.71	9.06×10^3	2.28	8.51×10^5	4.77		244	
		65.00	0.74	2.59×10^3	2.63	1.63×10^5	4.73		262	
		69.00	0.80	7.79×10^2	2.46	6.20×10^4	3.24		282	

deterioration of the current efficiency of the device. Several groups have utilized the $C–F$ technique with or without equivalent circuit simulations to explain the operational mechanisms of different OLED devices.[52] For instance, Kim *et al.*[54] recently utilized this technique without equivalent simulation to understand how different charge dynamics influence the lifetime in two distinct electron-transporting layers with the same EML OLED configuration and to grasp the significance of controlling the polaron density with the EML. In their investigations, the group compared a dopant-free EML device to a doped EML device and observed an increased capacitance at lower frequencies, which is a common phenomenon in $C–F$ analysis due to charge accumulation in the doped EML device compared to the dopant-free EML device.[52–54] This characteristic is attributed to the trapping/detrapping processes of holes in the dopant, resulting in increased capacitance at low frequencies in the device. However, as previously mentioned, this review focuses on the interpretation of $C–F$ simulations using equivalent circuits as an investigation tool from some pioneering groups.

3. Charge transport and accumulation in OLEDs

The kinetic processes of polarons in an EML are a result of the transportation of charges (holes and electrons) from the electrodes through the transporting layers, which later converge in the EML as voltage is applied.[55–58] This is analogous to the flow of two distinct fluids (charges) through opposite pipes into a barrel, as schematically shown in Fig. 5(a). Intuitively, the energy barrier at the interfaces in an OLED device adversely affects the free flow of these charges into the EML, thereby attenuating the device efficiency.[59–61] Emphasis has also been placed on the fact that molecular orientation also inhibits the flow of these charges.[62–64]

These characteristics are ubiquitous in research. For instance, Noguchi *et al.*[65,66] used IS to characterize the effect of polarized electron-transporting layer (ETL) molecules on the electrical properties of a bilayer device. The group emphasized that the correct dipole orientation in the small molecules of the ETL can either enhance or impede the injection of holes or electrons into the device, where these charges accumulate on the surface of the dipole and can only be transported after overcoming the energy potential of the dipoles. This investigation unequivocally proves that the dipole orientation in organic molecules can either increase or decrease the energy-level barrier, depending on the alignment direction of the PDM in the organic layers. Therefore, understanding these mechanisms in devices consisting of polar or nonpolar molecules (molecules with or without SOP, respectively) can inform the manipulation of organic devices to achieve high efficiency.[56,67,68] Fig. 5(b) shows a schematic of the charge injection, transport, and accumulation mechanisms through the transport layers before converging in the EML. This implies that efficient charge injection and transportation mechanisms are germane to achieving high efficiencies in OLEDs. Fig. 5(c) presents schematic diagrams illustrating the different molecular orientations corresponding to commonly used organic molecules and their chemical structures.

Equivalent circuit simulations as tools for investigating charge injection and energy barriers at interfaces have been reported by several groups. Iwamoto *et al.*[69] investigated the charging behavior of an OLED device with poly(3,4-ethylenedioxythiophene):poly(4-styrenesulfonate) (PEDOT:PSS) as the electrode (anode) and compared its characteristics with those of conventional indium tin oxide (ITO). In the group's investigation, certain characteristic regimes of the devices with respect to charge injection, transportation, and accumulation at designated voltages are described in the capacitance–voltage ($C–V$) curve, as shown in Fig. 6(a). These regimes are as follows: (1) the geometric capacitance
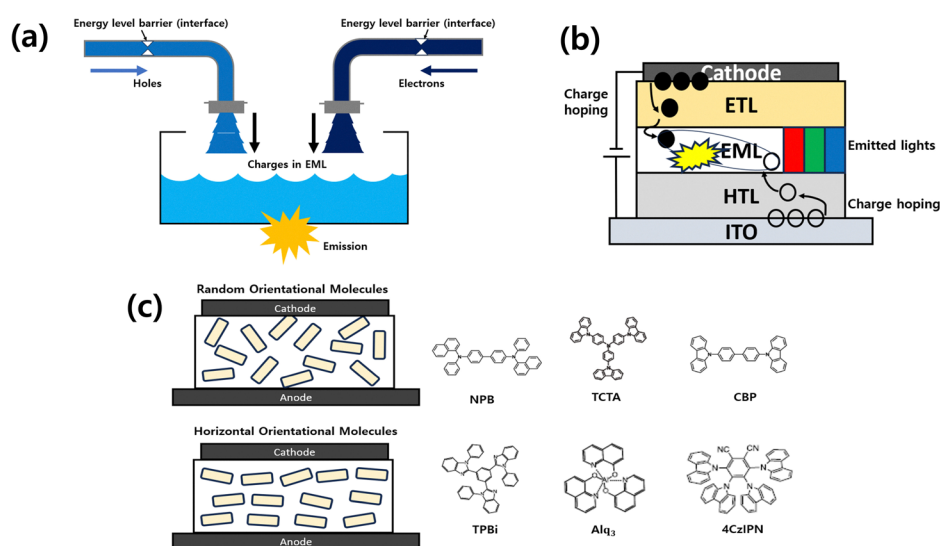

Fig. 5 Schematic diagrams. (a) Illustration of the flow of distinct fluids (charges) from opposite pipes into a barrel. Reproduced with permission from ref. 55 Copyright 2023, Wiley-VCH. (b) The charge injection, transportation, accumulation, and recombination in an OLED device. (c) The molecular orientation in some commonly used organic molecules and their chemical structures.
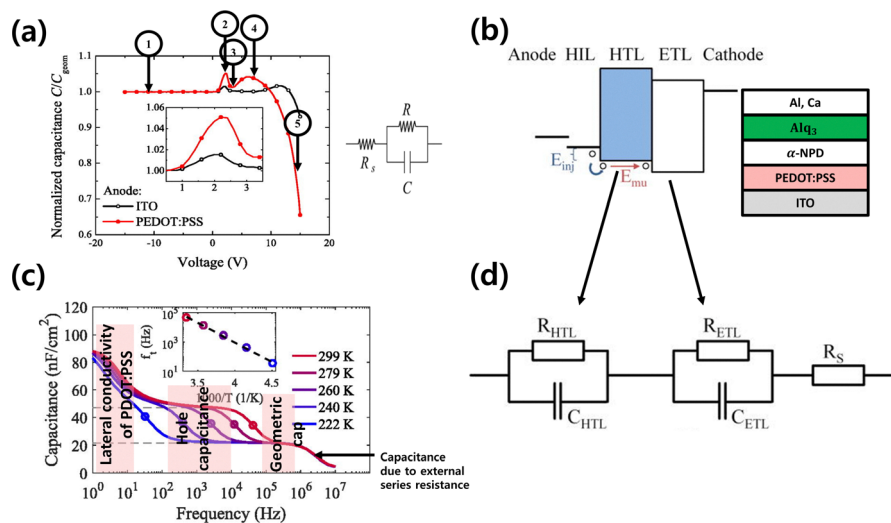
Fig. 6 (a) The capacitance–voltage curves of the OLED devices using ITO or PEDOT:PSS anodes at 1 kHz. Reproduced with permission from ref. 69 Copyright 2015, AIP Publishing. (b) The investigated device structure and its energy-level diagram with different anodes. Reproduced with permission from ref. 74 Copyright 2017, AIP Publishing. (c) The capacitance–frequency measurement at varied temperatures for the device structure at 0 V. Reproduced with permission from ref. 74 Copyright 2017, AIP Publishing. (d) The corresponding equivalent circuit representation as a series of two RC-circuits and a series resistance. Reproduced with permission from ref. 74 Copyright 2017, AIP Publishing.

of the device where no charge injection occurred, and (2) the increase in the capacitance due to charge injection localized around the electrode (anode). This is to assert that this group acknowledged the injection of holes first into the device prior to electron injection due to the SOP features of the ETL; (3) the decreased capacitance was due to the transport of charges (holes) into the organic layer to achieve a flat-band condition; (4) the capacitance increased again due to various mechanisms such as charge trapping; and (5) finally, the remarkable recombination of the electron–hole pairs decreased the capacitance after electron injection. These are common regimes in typical OLED devices. The group proceeded to investigate the devices through the frequency-dependent impedance magnitude and phase spectra at different voltages, and further simulated these data using the equivalent circuit presented in Fig. 6(a). The modeled equivalent circuit consists of a single parallel RC unit and a series resistance (R_s) representing the ITO or PEDOT:PSS electrodes under investigation. The frequency-dependent impedance magnitude and phase spectra simulated using the circuit fit well and generated information on the relaxation time (hole injection) and series resistance of the anodes. They pointed out that hole injection into the device using PEDOT:PSS as the anode was better than using ITO. A similar single parallel RC equivalent circuit unit was used to characterize the operational mechanisms of single-layered polymer emitting diodes.[70,71] Other studies reported the use of two parallel RC units to simulate single-layer device structures. For instance, Wu's group[72] used two parallel RC units to investigate the operational mechanisms of a single-doped layer OLED device. Their modeled equivalent circuit considered the bulk organic layer and depletion region at the cathode/organic layer interface. Iwamoto et al.[69] further modeled an equivalent circuit consisting of two (double) RC units and an R_s representing the double organic layers (hole- and electron-transporting layers, HTL and ETL) and the electrode to investigate the operational mechanisms of the full double-layer

device, including charge injection at the anodes, transportation, and accumulation at the interfaces. They pointed out that the injected holes from the PEDOT:PSS anode accumulated at the N,N'-bis(1-naphthyl)-N,N'-diphenyl-1,1'-biphenyl-4,4'-diamine (α-NPD)/tris(8-hydroxyquinoline)aluminum(III) (Alq$_3$) interface prior to electron injection for recombination to occur. This phenomenon is due to the SOP characteristics of Alq$_3$ which will be discussed in subsequent sections. The successful investigation of devices using an equivalent circuit indicates that the efficient charge injection properties of an anode are based on its energy-level alignment with the adjacent transporting layer.[73]

Brutting's group[74] also utilized the state-of-the-art C–F and equivalent circuit simulation technique to derive the hole mobility activation energy in the same polar OLED device structure (with PEDOT:PSS as an HIL) previously used by Iwamoto's group.[69] The investigated device structure is shown in (Fig. 6(b)). An equivalent circuit was modeled consisting of 2 RC units and an R_s representing the organic layers (HTL and ETL) and the contact resistance at the electrode and charge injection layer interface, respectively, as presented in (Fig. 6(d)). In their C–F measurement spectra at varied temperatures, different characteristics were observed at different frequencies which were attributed to the capacitance due to external series resistance (measuring equipment), geometric capacitance, hole capacitance, and lateral conductivity of the PEDOT:PSS layer as shown in (Fig. 6(c)). The modeled equivalent circuit was used to simulate the C–F spectra; however, the fittings were not accurate due to the parasitic capacitance (lateral conductivity of the PEDOT:PSS) not accounted for in the equivalent circuit model. Without any emphasis, the extracted values from the equivalent circuit were used to calculate the temperature-dependent transition frequency for hole injection using the formula in eqn (9).

$$f_t = \frac{1}{R_{HTL} \cdot (C_{HTL} + C_{ETL})} \tag{9}$$

where f_t, R, and C denote the transition frequency, resistance, and capacitance, respectively. They obtained the thermal activation energy of the hole current, as shown in the inset of (Fig. 6(c)) and the hole mobility activation energy using the Arrhenius eqn (10).

$$\mu(T) = \mu_0 \cdot \exp\left(\frac{-E_\mu}{k_B T}\right) \qquad (10)$$

where f_0, E_{act}, k_B, and T are the hole-relaxation frequency, activation energy, Boltzmann constant, and temperature, respectively. They also pointed out that holes were injected first into the device but accumulated at the α-NPD/Alq$_3$ interface prior to electron injection for recombination to occur. Moreover, the injection of hole charges is temperature-dependent.

In another case, W. Brutting's group previously utilized this technique to explain the charge injection and interfacial charge in an OLED device with a similar structure containing a polar material.[75] Fig. 7(a) shows the device structure, with Alq$_3$ recognized as a polar electron-transporting material. The group investigated the device in forward and reverse biases and demonstrated that holes were injected first into the device owing to the presence of negative interfacial charges (NICs) at the interface of Alq$_3$ as shown in the inset of Fig. 7(c). The geometric capacitance, hole injection based on the NIC, and electron injection regimes are described in the C–V curves in Fig. 7(c). In the C–F curve measurements shown in Fig. 7(b), the group observed two and three relaxation frequencies (f_r), which corresponded to the plateaus in the 0 V and 2 V spectra, respectively, at different frequencies and distinguished these f_r values according to the different characteristics occurring

within the device. Equivalent circuits consisting of two parallel RC units and R_s were modeled to represent each organic transport layer and electrode, respectively, within the device, as shown in Fig. 7(d). They first simulated the spectra using these circuits at different voltages but were only able to account for the hole capacitance at middle frequencies and the geometric capacitance and capacitance due to the measuring device at higher frequencies, as presented in Fig. 7(b). This indicates that the circuits in Fig. 7(d) do not fit the spectra well (the plateaus at lower frequencies were not considered). However, upon attaching additional double RC circuits that were attributed to a leakage current pathway within the device, as shown in Fig. 7(e), the simulation fitted the C–F spectra well and thus accounted for the plateau at lower frequencies, as shown in Fig. 7(b). Thus, the simulation results convey information on hole injection and accumulation prior to electron injection, which is due to the NIC, as well as the leakage current that occurred in the OLED device.

As this technique evolved, Lee et al.[37] also adopted it to investigate charge transport and accumulation in a mixed-host EML OLED, as shown in Fig. 8(a). The group modeled equivalent circuits shown in Fig. 8(c), consisting of three RC units and R_s representing each organic layer and the contact resistance, respectively, and used these to simulate the C–F curves at different voltages, achieving a good fit to the curves. Different equivalent circuit models were used to simulate the devices at different voltages. The attached RC units in series (simulation at 2.5 to 4 V) accounted for the traps in the device, which will be discussed in the subsequent section. The same strategy was reported by Data et al.,[76] where different circuits were used to estimate the mobility
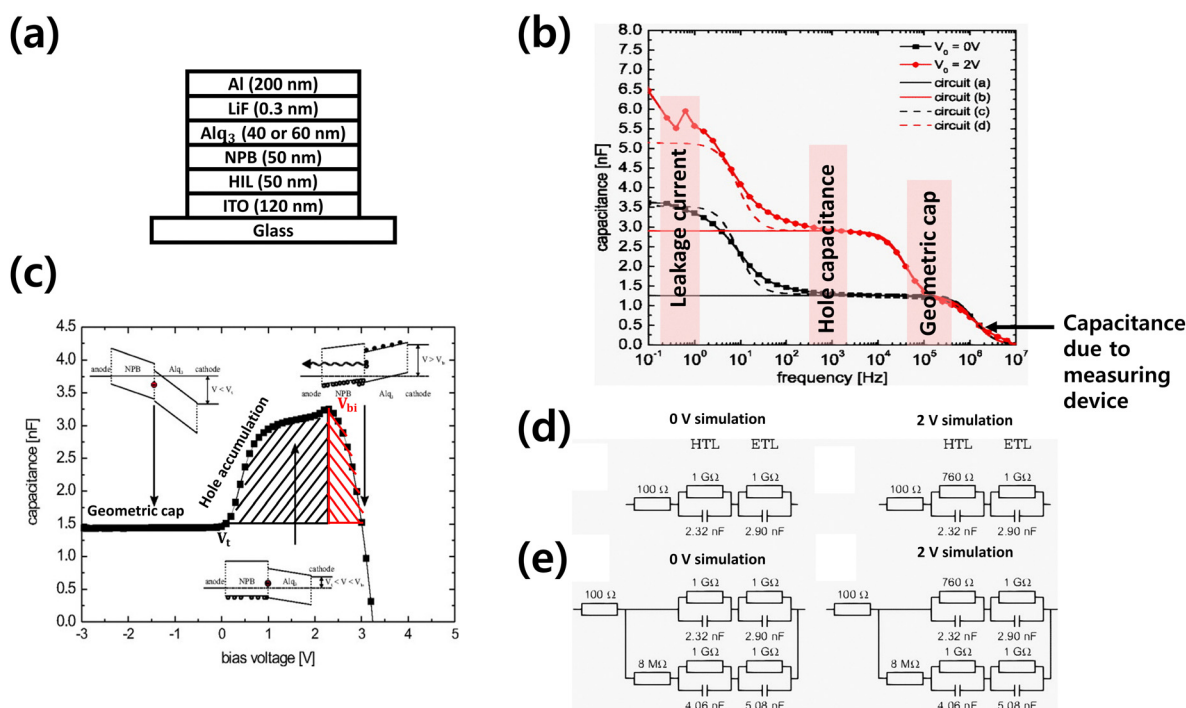

Fig. 7 (a) The structure of the investigated OLED device. (b) Capacitance–frequency measurements at different voltages. (c) Voltage-dependent capacitance characteristics curve of the OLED device. (d) Equivalent simulation circuits without an additional leakage current path. (e) Equivalent simulation circuits with an additional leakage current path. Reproduced with permission from ref. 75 Copyright 2010, AIP Publishing.
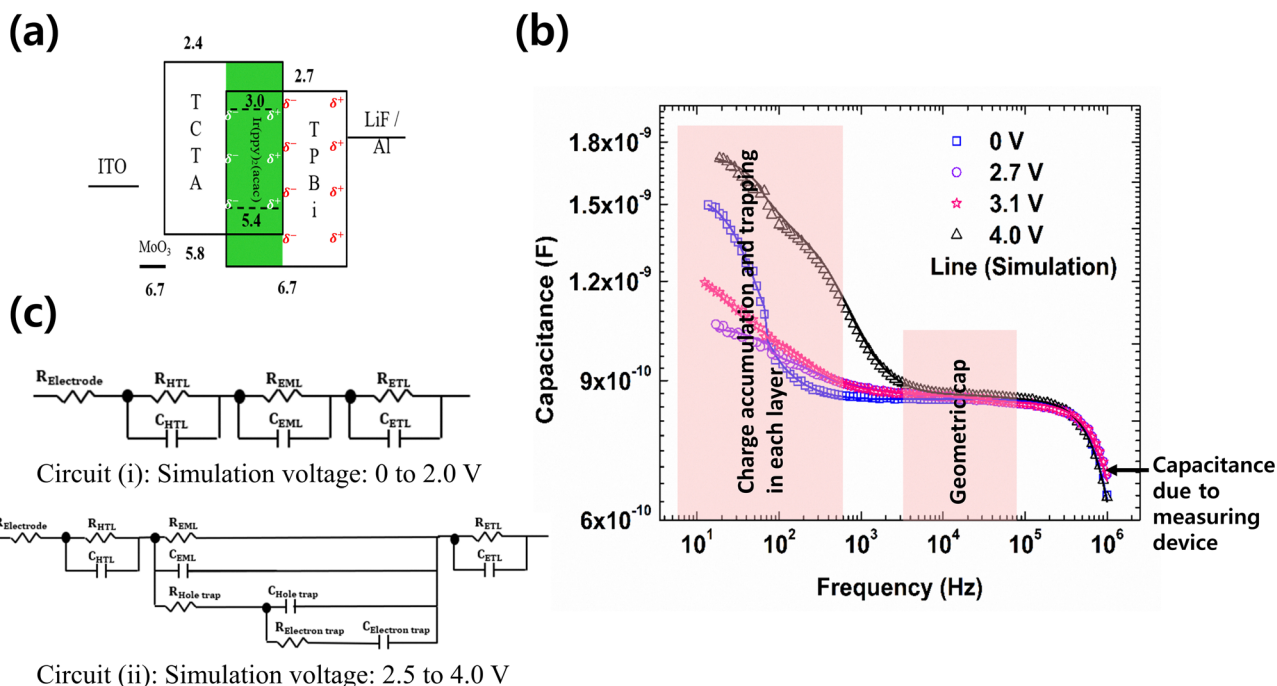
Fig. 8 (a) The schematic energy-level diagram of the mixed-host EML OLED device. (b) The capacitance–frequency measurement curves at different voltages. (c) Modeled equivalent circuits for different voltage simulations. Reproduced with permission from ref. 37 Copyright 2023, Elsevier Ltd.

and concentration of charge carriers in the transporting layers of OLED devices at different voltages. Lee *et al.*[37] considered the error parameters for the circuit choice, the distinct threshold voltage at which the first circuit switched to the second, and, most importantly, the structure of the device. In the *C–F* spectra of the group shown in Fig. 8(b), different characteristic curves are observed at different voltages. At 5 V, two plateaus corresponding to two relaxation frequencies were observed. These plateaus are attributed to charge accumulation and trapping in each organic layer at lower frequencies, geometric capacitance at middle frequencies, and capacitance of the measuring device at higher frequencies, as shown in Fig. 8(b). The extracted RC values at different voltages using the equivalent circuit simulation were plotted for each organic layer (Fig. 9(a)–(c)), detailing

the charge injection, transportation, and accumulation corresponding to the *C–V* characteristics of the device. They also adopted a polar electron-transporting material in their investigation and clearly described the operational mechanisms of a mixed-host EML device with such molecules. They also acknowledged the key point, that holes were first injected into the device prior to electron injection, owing to the presence of the NIC. The group further asserted that the efficient injection and transportation of charges into the EML was due to the absence of energy barriers, owing to the use of the same material as the mixed-host EML coupled with the presence of the NIC in the polarized 2,2′2″-(1,3,5-benzinetriyl)-tris(1-phenyl-1-*H*-benzimidazole) (TPBi) material. Thus, the *C–F* and equivalent circuit simulation techniques can be successfully utilized to quantitatively
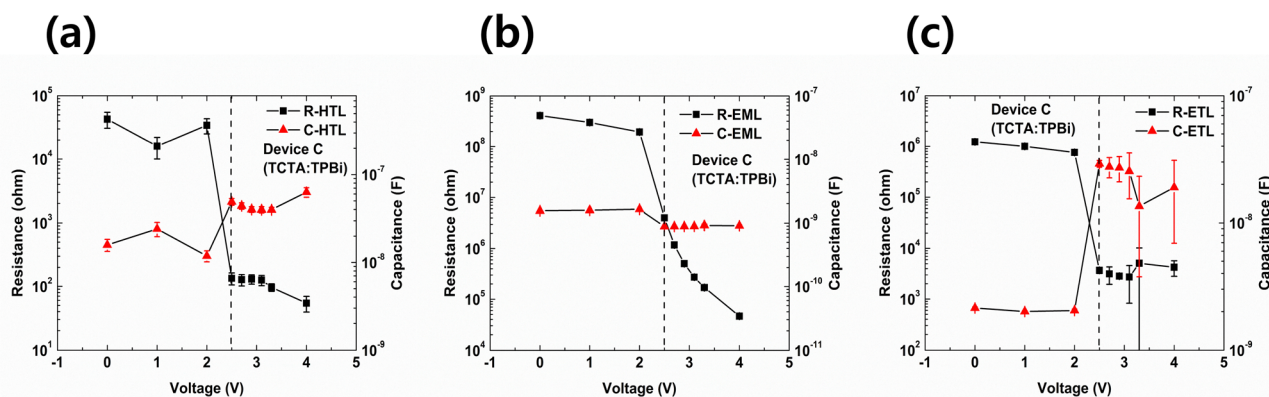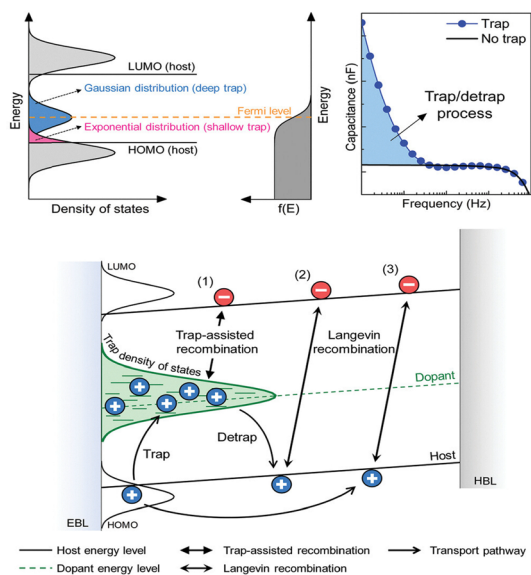

Fig. 9 Resistance–voltage–capacitance simulation results for each organic layer. (a) HTL, (b) EML, and (c) ETL. Reproduced with permission from ref. 37 Copyright 2023, Elsevier Ltd.

Fig. 10 Trap dynamics and recombination mechanisms: energy distribution of density of states (DOS) in the host and dopant with Fermi–Dirac distribution, the contribution of trap dynamics on the capacitance–frequency spectrum, and the schematic diagram illustrating the trap-assisted and Langevin recombination (γ_L) processes. Reproduced with permission from ref. 57 Copyright 2023, Wiley-VCH.

analyze charge injection, transportation, and accumulation in each organic layer.

4. Charge dispersion/traps in OLED devices

In recent years, the understanding of charge trap mechanisms in OLEDs has progressed significantly. This mechanism occurs

because of the different energy-level alignment between the host and dopants or at the organic–organic/organic–metal interfaces, limiting charge transport in organic semiconductors.[77,78] Fig. 10 illustrates the trapping/detrapping processes of charges in the dopant of an EML and how they contribute to recombination, their characteristics in a typical C–F graph, and the energy levels at which these phenomena occur. Based on the prevalence of trapping/detrapping mechanisms in organic devices, several groups have taken the initiative to utilize IS and equivalent circuits to investigate and understand these mechanisms and how they affect their operational mechanisms and electrical properties.

As a novel application of IS and equivalent circuit, Leo's group[79] investigated the charge carrier trap response and the type of traps present in a pentacene Schottky diode doped with fluorinated fullerene derivative ($C_{60}F_{36}$) and 2,2′-(perdiylidene)di-malononitrile (F_6-TCNNQ). They investigated devices using frequency–dependent capacitance characteristics with respect to different dopants. In their C–F curve, shown in Fig. 11(a), they observed an additional capacitance contribution at lower frequencies ($<10^2$ Hz), which was attributed to the presence of deep trap states in the doped pentacene material. At low frequencies, the trap states followed the applied frequency modulation, and an additional capacitance contribution was observed. A single-layer equivalent simulation circuit, as shown in Fig. 11(b), which corresponds to the doped pentacene layer, was modeled while considering the presence and absence of charge traps, as well as the type of traps (Gaussian and exponential trap states) present in the doped layer. The circuit without the impedance trap unit (Z_t) did not fit the C–F curve well at lower frequencies compared with the circuit with the trap unit. Moreover, considering the types of traps present in their modeled equivalent circuit, the modeled circuit accounting for Gaussian trap states fitted the C–F curve better than the exponential trap states, as shown in Fig. 11(a). Their investigation revealed that deep Gaussian
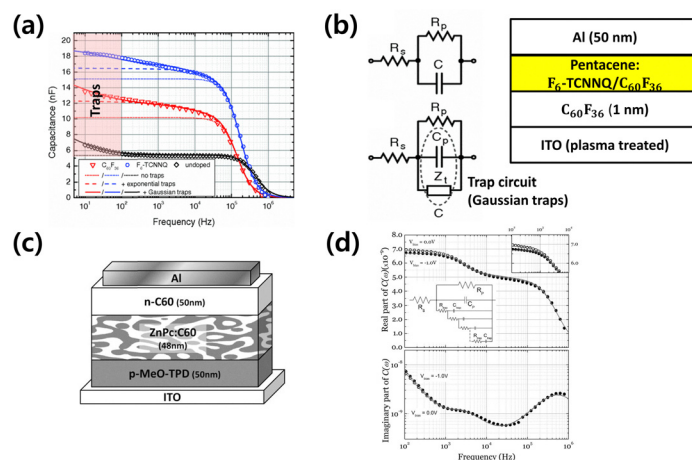
Fig. 11 (a) Capacitance spectra of pentacene Schottky diodes, comprising 0.5 wt% each of $C_{60}F_{36}$ and F_6-TCNNQ dopant molecules and the undoped device at 0 V. Reproduced with permission from ref. 79 Copyright 2013, American Physical Society. (b) The applied equivalent circuit models, with and without the trap distribution element (Z_t) for simulating the capacitance–frequency dependent spectra and the device structure. Reproduced with permission from ref. 79 Copyright 2013, American Physical Society. (c) Structure of the solar cell device (ZnPc:C60 bulk heterojunction as the photo-active layer). Reproduced with permission from ref. 80 Copyright 2012, AIP Publishing. (d) The real and imaginary parts of the complex capacitance at 0 V and −1.0 V bias. Reproduced with permission from ref. 80 Copyright 2012, AIP Publishing.
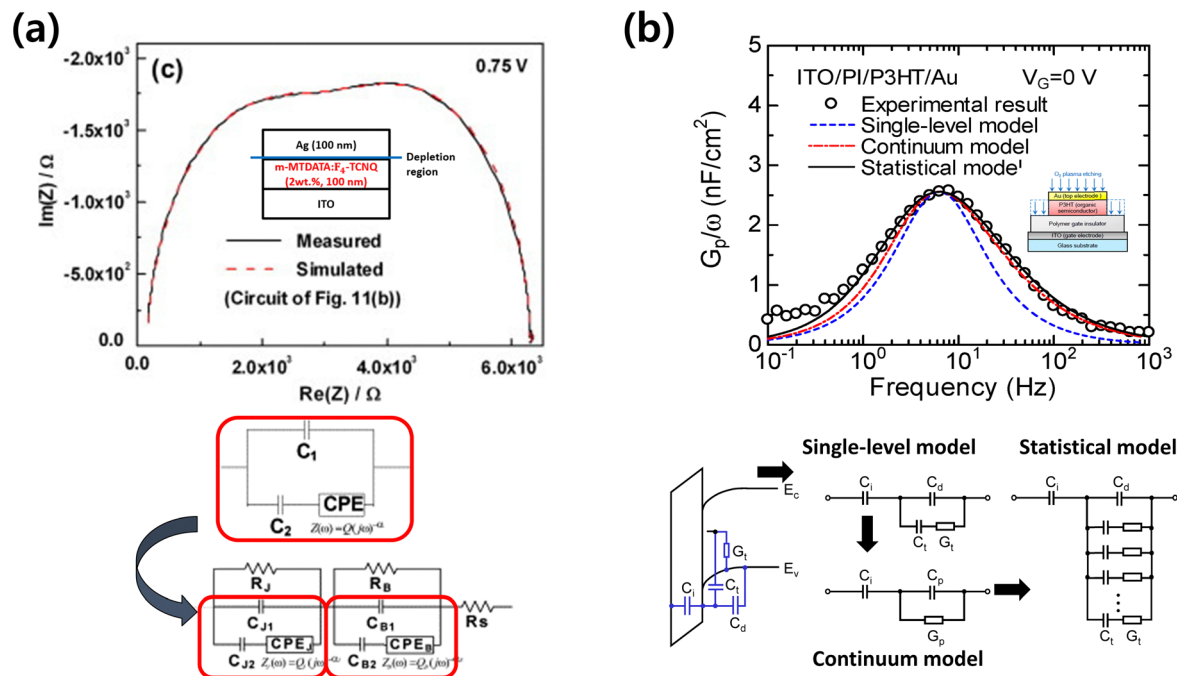
Fig. 12 (a) The optimized fitting to the measured Cole–Cole plot at 0.75 V using the equivalent circuit for a material and depletion layer having a dispersive dielectric response. Reproduced with permission from ref. 72 Copyright 2010, Elsevier Ltd. (b) Plot of the equivalent parallel conductance loss *versus* frequency for the organic transistor at 0 V and equivalent circuit comprising the single-level, continuum, and statistical simulation models. Reproduced with permission from ref. 81 Copyright 2018, MDPI.

trap states were the dominant trap states in the doped pentacene. Further investigation into the density of traps, which was performed through calculations using the parameters extracted from the equivalent circuit, revealed the presence of higher trap states in pentacene doped with F_6-TCNNQ, which increased with the doping ratio. Leo *et al.*[80] also investigated the response and energy distribution of trap states in organic solar cells. The structure of the device is presented in Fig. 11(c). Similarly, the additional capacitance at lower frequencies ($<10^3$ Hz) was attributed to the presence of traps in the device in the measured *C–F* curve, as shown in Fig. 11(d). A repetitive RC circuit in series attached to a single parallel RC unit, as shown in the inset of Fig. 11(d) was modeled to simulate the *C–F* of the device. The single parallel RC unit and the repetitive RC circuit in series corresponded to the bulk zinc–phthalocyanine (ZnPc:C_{60}) and the energetic distribution of the trap states within the bulk material, respectively. A good fit of the experimental *C–F* curve was obtained, and the extracted parameters (presented in Table 2) from the equivalent circuit were used to estimate the trap density in ZnPc:C_{60} as $1.9 \pm 0.6 \times 10^{16}$ cm^{-3} eV^{-1} using eqn (11).

$$C_{\text{traps}} = A\sqrt{qg_0\varepsilon} \tag{11}$$

where C_{traps} is the elementary capacitance value, A is the area, q is the charge, g_0 is the trap density, and ε is the dielectric constant.

An investigation conducted by Wu *et al.*[72] characterized a conductively doped organic hole-transporting layer (4,4′,4″-tris(3-methylphenylphenylamino)triphenylamine (m-MTDATA)) and modeled a CPE in series with a capacitor in their double RC equivalent circuit, which accounted for dispersive properties

such as spatial inhomogeneities, dopant concentration, and traps in the organic layer and depletion region to fit their experimentally measured Cole–Cole plot. Their results, after a good fit to the Cole–Cole plot, as shown in Fig. 12(a), revealed that these dispersion properties are present not only in the bulk organic layer but also in the depletion region. This successful investigation informs the use of IS and equivalent circuit techniques as tools to locate trap regions in an OLED device. Considering the location of traps in organic semiconducting devices, Naito *et al.*[81] reported the presence of interfacial traps in an organic field-effect transistor (FET). They indicated that these trap states were energetically distributed at the interface. The group made this conclusion based on a simulation of the conductance–frequency spectrum of the device using the statistically modeled circuit presented in Fig. 12(b). Their equivalent circuit was a cascading sequence of capacitance and conductance in series, representing the trap states attached to the capacitance of the doped layer. In summary, the statistically modeled equivalent circuit, while taking into consideration the band-bending fluctuations, fitted the conductance characteristic curve of the device well, confirming that energetically distributed trap states can be present at the interfaces.

As mentioned previously, Lee *et al.*[37] also adopted IS and equivalent circuit simulation techniques to investigate traps in a mixed-host EML OLED. Their modeled trap equivalent circuit, as shown in Fig. 8(c), is similar to that of Leo's previous approach,[80] as shown in Fig. 10(d); however, the group focused on quantitatively determining the capacitance of the holes and electrons trapped in the dopant of the EML. Notably, the
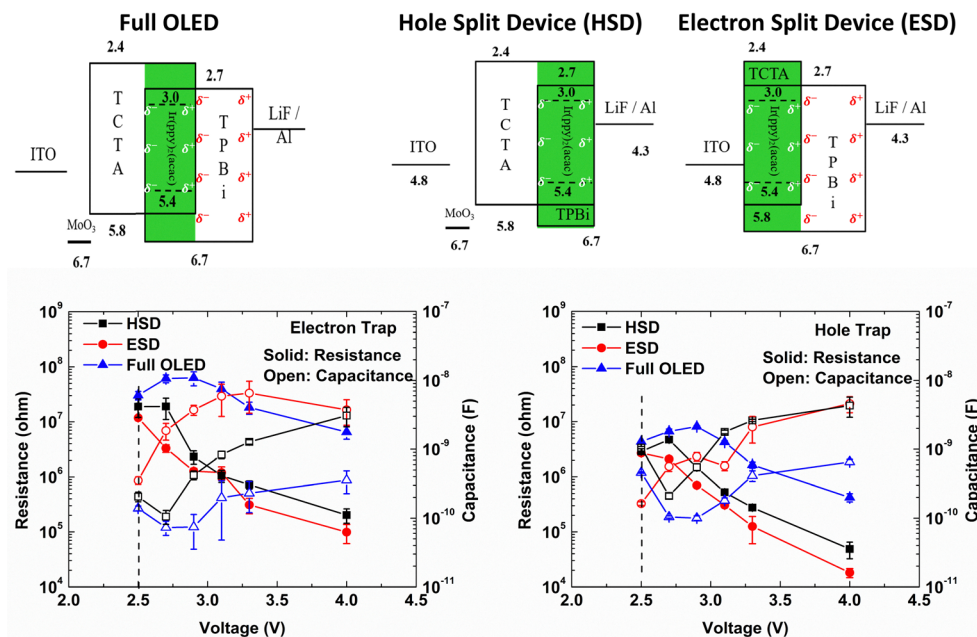
Fig. 13 Energy-level diagrams of the fabricated devices (Full OLED, HSD and ESD) and the simulated trapped electrons and holes in the dopant of the EML. Reproduced with permission from ref. 37 Copyright 2023, Elsevier Ltd.

modeled equivalent circuits by both groups[37,79,80] were executed using commercial simulation tools. Two equivalent circuits were used to simulate the C–F spectra of the mixed-host EML devices at different voltages. The latter, which is the equivalent trap simulation circuit at 2.5 to 4.0 V, as shown in Fig. 8(c) was modeled due to the anticipation of the response of traps at these voltages. The group reported that the dopant in the EML served as the electron and hole trap site, enabling the occurrence of trap-assisted recombination concurrently with Langevin recombination (γ_L) in the host EML. This was also observed by other groups[54,82] and was recently reported by

Lee et al.,[57] illustrating the mechanisms of various recombination processes, as schematically illustrated in Fig. 10. These groups also suggested that trap-assisted recombination occurred only between trapped holes and electrons (process 1). They further explained that the surplus trapped charges in the trap states could be detrapped toward the HOMO level of the host and recombined with free electrons (process 2). However, Langevin recombination occurs directly between the injected holes and electrons in the host (processes 2 and 3). A well-fitted simulation of the C–F curve at different voltages was performed using Lee et al., who defined the use of the trap circuit at higher
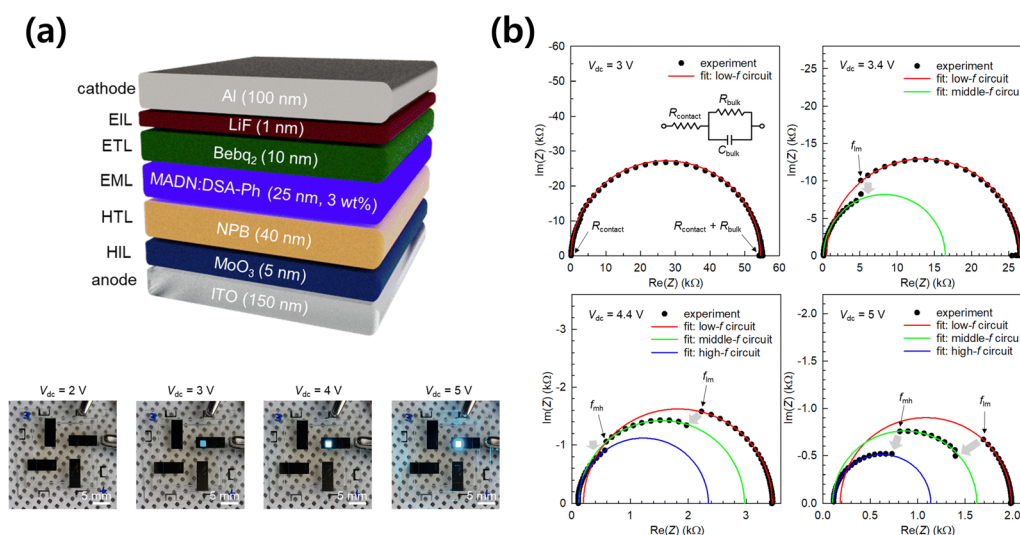
Fig. 14 (a) The schematic illustration of the OLED structure and the photographs showing the gradual switching and brightness emission of the fabricated OLED. (b) Cole–Cole plot of the OLED measured at 3 to 5 V. Reproduced with permission from ref. 83 Copyright 2023, Royal Society of Chemistry.

voltages, which enabled the successful quantitative determination of the capacitance of charge traps in the mixed-host EML, as shown in Fig. 13.

Although these techniques have been in use for several years, they are still used to investigate modern devices with sophisticated structures. For instance, Kim et al.[83] recently investigated frequency-triggered circuit transition in an OLED device as a new potentially applicable AC regime phenomenon. The group investigated these frequency-triggered transitions using a single equivalent circuit comprising the contact resistance in series and the RC of the bulk material in parallel. The structure of the device and modeled equivalent circuit are shown in Fig. 14(a) and the inset of Fig. 14(b), respectively. The group pointed out that the abrupt frequency-triggered responses observed at different voltages (3.4 to 5 V) in the Cole–Cole plot were due to the electrical trapping and detrapping of charges in the dopant molecules of the device as the frequency varied (decreased), as shown in (Fig. 14(b)). These trapping and detrapping phenomena were also reported by Kim et al.[54] in their investigations, who reported that the trapping and detrapping of holes in the dopant resulted in increased capacitance in the low-frequency region. Kim et al.[83] asserted that the trap states in an OLED with different reaction speeds can lead to the observed frequency-triggered internal transitions. They further explained that at low frequencies, all trapped charges had sufficient time to be electrically charged and discharged, leading to the largest bulk resistance and the most extended impedance (Z) footprint. However, upon a gradual increase in frequency, the dropped characteristics of the Cole–Cole curve at frequencies denoted as f_{lm} and f_{mh} (3.4 to 5 V) indicate that each grouped trap stopped responding to the applied voltage and became deactivated, leading to the abrupt shrinking of the complex impedance curve. These results underscore the reliability and accuracy of IS and equivalent circuit techniques for investigating traps in OLED devices.

5. Degradation in OLED devices

It has been stipulated that the detrimental effects of degradation in OLED devices could be a result of excess accumulation of charges in the organic layers/interfaces and traps,[84–87] depletion of dopant concentration,[88] depletion of SOP,[89,90] recrystallization,[91,92] temperature conditions etc.[53,93]

Lee et al.[88] reported the degradation mechanism in a charge-generation layer (CGL) device, as shown in Fig. 15(a), using IS and equivalent circuits. In their measured C–F curve, the group observed a capacitance reduction of approximately 19.6% after aging at 100 kHz (Fig. 15(a)). By leveraging the equivalent circuit technique, the C–F spectra of the pristine and aged devices were simulated under reverse and forward biases using the equivalent circuits presented in Fig. 15(b). Two (2) RC units corresponding to the combined intrinsic and doped layers were used to simulate the spectra in the reverse bias while three (3) RC units corresponding to the combined intrinsic, depletion, and doped layers were used to simulate the spectra in the forward-bias region. In the forward-bias region, a depletion region is expected at the p–n junction, which enables charge tunneling. The group pointed out that the significantly increased resistance and decreased capacitance in the doped layers after aging, as shown in the resistance and capacitance–voltage dependent plot of the parameters (presented in Table 2) obtained from the simulation of the pristine and aged CGL devices, were due to the lower charge generation in these layers. This indicates that the doped organic layers are the main contributors to the degradation of OLED devices. Consequently, an optical spectroscopy analysis was conducted to confirm that the degradation mainly occurred in the doped TPBi rather than the doped N,N'-di(1-naphthyl)-N,N'-diphenyl-(1,1'-biphenyl)-4,4'-diamine (NPB) layer, due to the decomposition of its dopant.

Interestingly, Kim's group[94] also conducted a lifetime assessment of an OLED using IS and an equivalent circuit, as well as a deep machine learning technique. The ETL of the device structure was also formed from TPBi, as shown in Fig. 16(a). Recall that TPBi is a polarizing material. Three (3) RC units, as shown in the inset of Fig. 16(b) were modeled based on the curvature calculations from the Cole–Cole IS plot and its fitting results were plotted as the relaxation time plot for each transporting layer (Fig. 16(c)), using eqn (1). The obtained relaxation times in descending order ($\tau_{p1} > \tau_{p2} > \tau_{p3}$) correspond to the charge accumulation at the
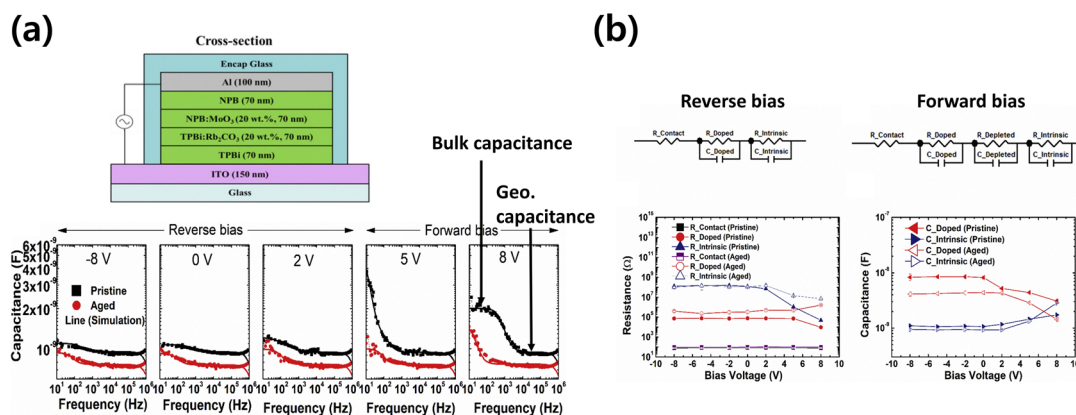

Fig. 15 (a) Schematic structure of the CGL device and the capacitance-frequency plot for the pristine and aged devices in the reverse and forward bias. (b) The equivalent circuit models for the reverse- and forward-bias simulation as well as the resistance and capacitance–voltage dependent plot of the parameters obtained from the simulation of the pristine and aged CGL devices. Reproduced with permission from ref. 88 Copyright 2021, Elsevier Ltd.
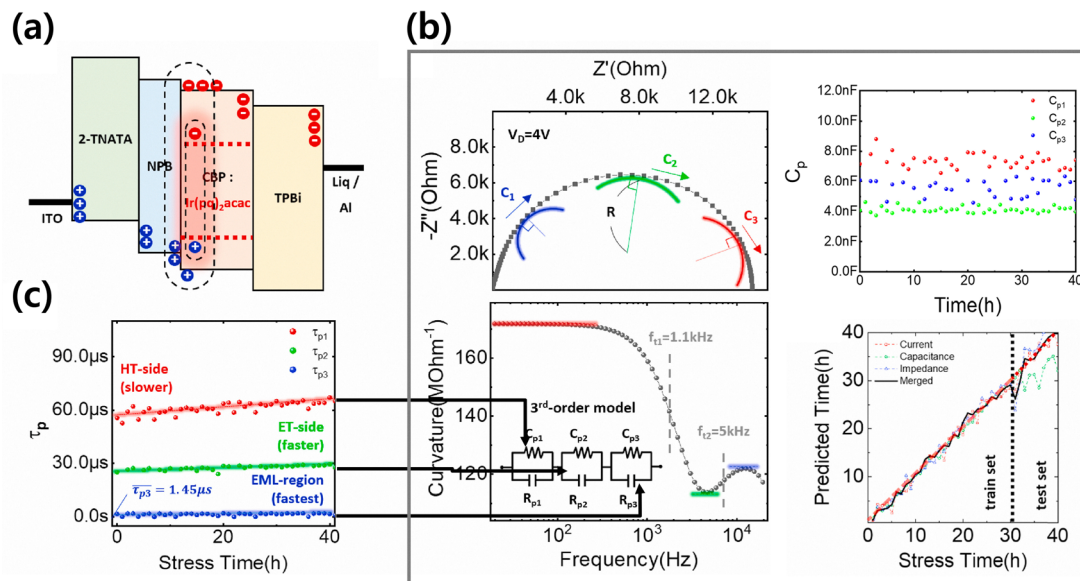
Fig. 16 (a) Energy band diagram of the fabricated OLED. (b) Cole−Cole impedance plot, curvature−frequency dependent plot, capacitance−time plot, and lifetime prediction of each feature and merged feature. Inset: The modeled equivalent circuit. (c) Relaxation time during accelerated stress test for 40 hours. Reproduced with permission from ref. 94 Copyright 2022, Elsevier Ltd.

hole transport region, electron transport region, and emission region, respectively, as schematically shown in Fig. 16(a). During the monitoring stage of 40 h at 4 V, the group observed a gradual increase in the relaxation time in each organic layer, which corresponded to an increase in the resistance and subsequent degradation in these organic layers, as shown in Fig. 16(c). Further

investigations revealed that the increased degradation in these organic layers was due to trapped charges. In fact, the increased resistance was reported to be the dominant parameter affecting the relaxation frequency because the capacitance was constant at all aging times, as shown in Fig. 16(b). The group proceeded to predict the lifetime of the OLED device using machine learning
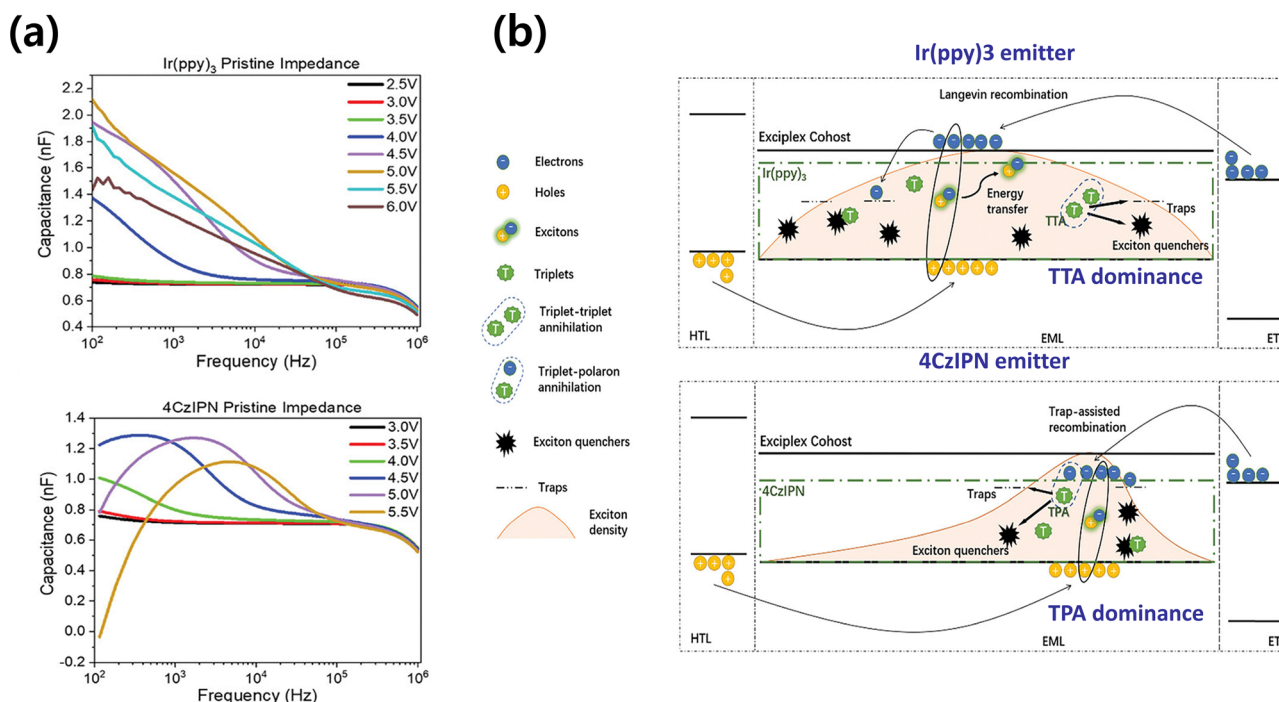
Fig. 17 (a) Capacitance−frequency plot of the Ir(ppy)$_3$- and 4CzIPN-based devices. (b) TTA and TPA degradation and quenching mechanisms in a phosphorescent emitter (Ir(ppy)$_3$) and thermally activated delayed fluorescent emitter (4CzIPN), respectively. Reproduced with permission from ref. 58 Copyright 2024, Wiley-VCH.

Fig. 16(b), which enabled faster and more accurate predictions of the lifetime of the device. This observation indicates that the intrinsic TPBi can also undergo degradation without doping. The pronounced increase in the relaxation time of the HTL side after aging was due to the combined characteristics of the two HTLs. Some groups have also reported that the degradation of OLED devices is mainly due to mechanisms such as triplet–triplet annihilation (TTA) and/or triplet-polaron annihilation (TPA) owing to the accumulated holes or electrons in the EML.[95] These were recently reported by Lee et al.,[58,95] who leveraged IS as a tool to investigate the degradation.

behavior in phosphorescent and thermally activated delayed fluorescent OLEDs using their respective common green emitters (Ir(ppy)$_3$ and 4CzIPN). The group demonstrated that in both emitters, the energy-level offset between the host and dopant resulted in trap formation in the EML. This was linked to their observed short lifetimes, indicating that the trapped holes or electrons led to the narrowing of the effective recombination zone and induced TPA or TTA, which triggered charge trap formation, charge imbalance in the localized emission zone, and accelerated device degradation. These characteristics are also evident in the C–F spectra at low frequencies, with increased capacitances for both dopants, as shown in Fig. 17(a). However, a disparity was obvious; in the Ir(ppy)$_3$-based device, a continuously increasing capacitance was observed, indicating the detrapping of some trapped holes into the host, which contributed to the overall capacitance, whereas in the 4CzIPN-based device, a negative capacitance appeared after 5 V, which was attributed to trap-assisted recombination in the device. This implies that TTA is dominant in phosphorescent emitters, whereas TPA is dominant in TADF emitters, as schematically illustrated in Fig. 17(b). Similar characteristics were also

reported by Brutting et al.,[96] who used displacement current measurement (DCM) and time-resolved electroluminescence spectroscopy (TrEL) to investigate degradation in an OLED device. The group asserted that the trapped holes in the EML served as triplet-polaron quenchers, thereby degrading and decreasing the luminance of the device.

Further studies have recently reported on the thermal degradation and stability of organic devices to ascertain the cause of this detrimental effect. Lee et al.[91,92] investigated the thermal degradation and stability of an organic homojunction consisting of an intrinsic organic layer and a molybdenum oxide (MoO$_3$)-doped organic layer under thermal heating (annealing) using the device structures; the corresponding chemical structures of the organic molecules are shown in Fig. 18. Their measured impedance-frequency-dependent graphs, as shown in Fig. 19(a) and (c), were simulated using the modeled two RC equivalent circuit units, as shown in the inset of Fig. 19(a), where R_s, parallel $R_d C_d$, and parallel $R_i CPE_i$ represent the series resistance, MoO$_3$-doped organic layer, and intrinsic layer, respectively. The extracted parameters presented in Table 2 were plotted to determine the electrical characteristics of each organic layer, as shown in Fig. 19(b) and (d). From the results of the NPB-based device shown in Fig. 19(b), the decreased resistance at higher temperatures in the doped and intrinsic layers was postulated to be due to either the diffusion of dopants into the intrinsic layer or the recrystallization of the intrinsic layer. However, the former was refuted based on optical analysis, which confirmed the absence of dopant diffusion into the intrinsic layer at higher temperatures. Similar observations were made in the 4,4′, 4″-tris(N-carbazolyl)-triphenylamine (TCTA)-based device, as shown in Fig. 19(d). This observation was attributed to the crystallization of the intrinsic molecules, which was subsequently confirmed in an ultraviolet
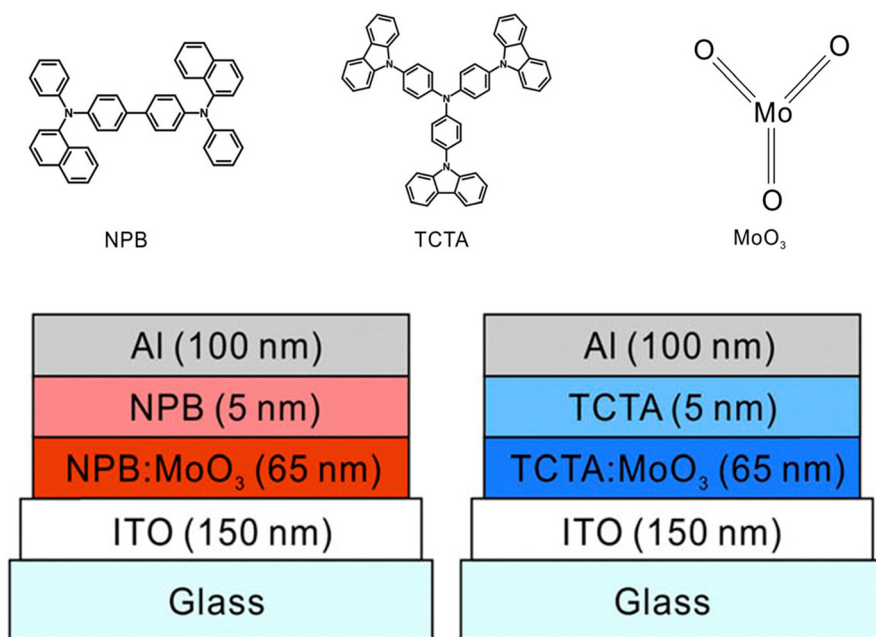

Fig. 18 Chemical structures of the organic molecules and the schematic structures of the fabricated devices. Reproduced with permission from ref. 92 Copyright 2020, AIP Publishing.
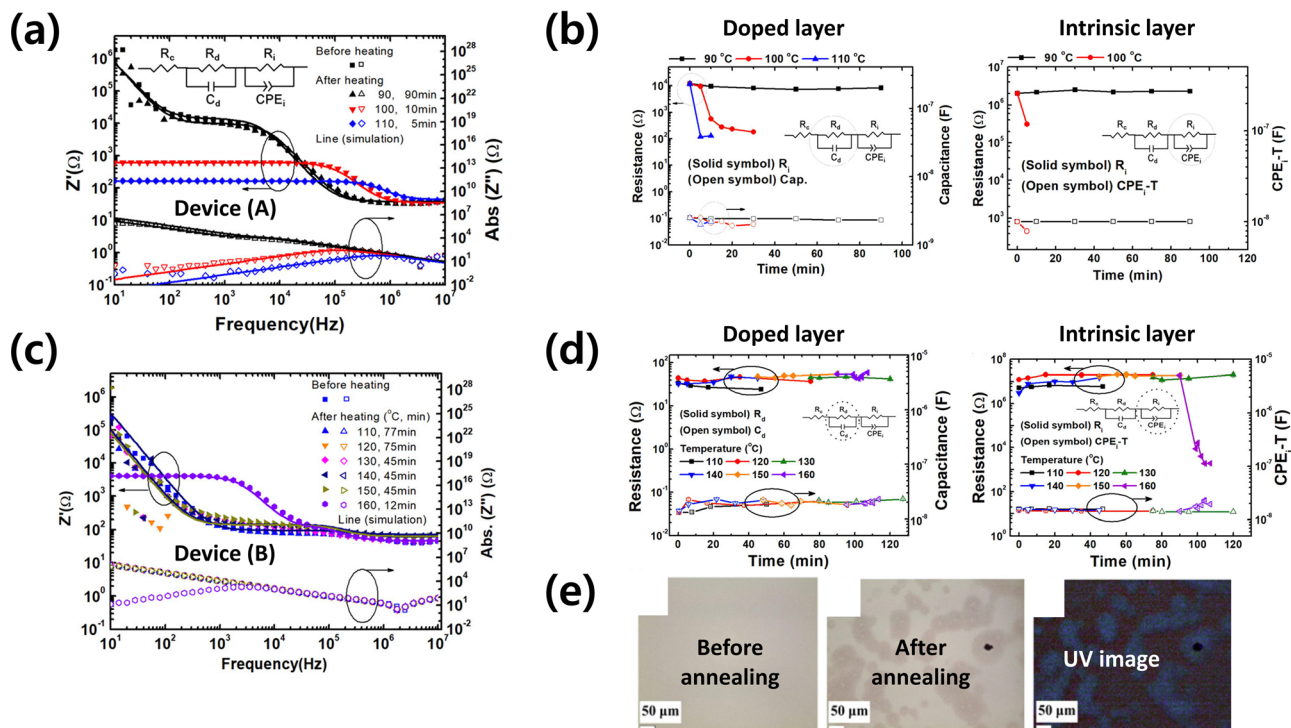
Fig. 19 (a) The impedance-frequency characteristics of the device (A) annealed at different temperatures. (b) The resistance, capacitance, and CPE parameters of device (A) as a function of annealing temperature. (c) The impedance-frequency characteristics of the device (B) annealed at different temperatures. (d) The resistance, capacitance, and CPE parameters of device (B) as a function of annealing temperature. (e) Optical microscopy images of an intrinsic TCTA-based device. Reproduced with permission from ref. 92 Copyright 2020, AIP Publishing.

(UV) image analysis as an uneven distribution of these crystalline molecules, as shown in Fig. 19(e).

6. Other impedance spectroscopy techniques

So far, charge transport and accumulation, charge trapping, and degradation in OLED devices have been investigated using IS comprising capacitance–frequency simulations with equivalent circuits. IS is a broad concept not limited to equivalent circuit analysis. There are different representations of IS dataset, including impedance [Z] Cole–Cole, real impedance (Re[Z])–frequency, modulus [M] Cole–Cole plot, imaginary part of complex modulus [M]–frequency, Re[Z]–voltage, C–V simulation $etc.$, which are adopted to investigate the operational mechanisms in OLED devices without factoring in the equivalent circuit simulation. Some of these impedance spectra are analyzed or sometimes simulated using pre-existing or derived complex equations to derive parameters such as mobility, charge density, and traps.[97,98]

For instance, Naito $et\ al.$[99] developed a numerical model to determine the localized state distribution (traps) and drift mobility based on the theory of single-injection space-charge-limited current in single-charge polymer-based OLED devices. Their model was validated by calculating the localized state distribution below the conduction band (E_c) and above the valence band (E_v) from the conductance and capacitance of electron- and hole-only devices (EOD and HOD) at different

temperatures. The structures of the devices and the calculated localized energy-state distributions and densities are presented in Fig. 20(a). They pointed out that the trap-captured states within the energy range of 0.3–0.8 eV, below E_c and above E_v, are independent of energy levels since their calculated localized state distribution fell on the same line at different temperatures. They further demonstrated shallow traps at 170 K and deeper traps at 350 K in the conduction band, whereas shallow traps were measured at 150 K and deeper traps were measured at 480 K in the valence band. The same model was extended to confirm the independent trap states on the energy levels during their investigation of charge carrier mobility, distribution of localized states, and deep trapping lifetime in a single-charge small-molecule-based OLED device.[100] Another comprehensive study was conducted using the proposed model from the same group[101] to investigate the bimolecular recombination constant (β) in a double-injection polymer-based OLED device (poly(9,9-dioctylfluorene-alt-benzothiadiazole) (F8BT). The group observed a lower recombination constant compared with that of the Langevin recombination (β at 300 K and 130 kV cm^{-1} is 9.8×10^{-13} cm^3 s^{-1}, which is approximately 10^2 times smaller than γ_L), which was determined from the charge mobilities and susceptance plot in Fig. 20(b) and the inset of Fig. 20(b), respectively, based on the model. This demonstrates that the proposed numerical model in the IS is another viable technique for probing charge mobility in OLED devices.

Modulus Cole–Cole plot analysis is another type of IS representation used to investigate OLED devices. It represents the dielectric characteristics as a function of frequency in polar
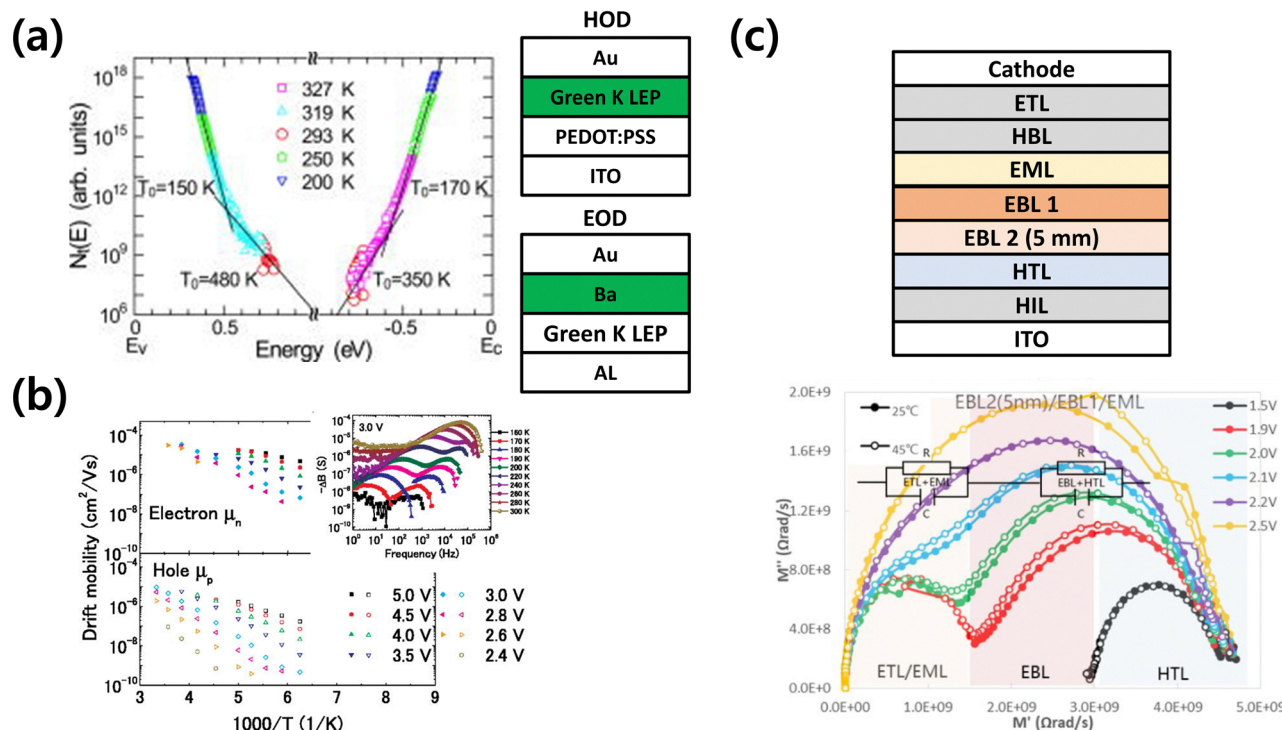
Fig. 20 (a) The trap distributions in the energy gap of the hole-only device (HOD) and electron-only device (EOD) alongside their structures. Reproduced with permission from ref. 99 Copyright 2009, AIP Publishing. (b) The plots of electron and hole drift mobilities *versus* temperature at different voltages in the F8BT-based OLED (inset: frequency dependence of the negative susceptance at different temperatures). Reproduced with permission from ref. 101 Copyright 2019, AIP Publishing. (c) The modulus Cole–Cole plot at 25 °C and 45 °C, at different voltages, including an equivalent circuit and its schematic device structure. Reproduced with permission from ref. 104 Copyright 2024, Wiley-VCH.

coordinates for characterizing OLED devices. Just above the turn-on voltage, the modulus Cole–Cole plot mostly shows two or more completely independent semicircles, which quantitatively reveal when charges are injected into the device. The diameter of the semicircle in the modulus plot is inversely proportional to the capacitance of the injected charge; thus, the observed change (increase and merger) in the formation of the semicircle at increasing voltages reveals the injection and flow of holes and electrons in the device.[102] This technique is similar to the complex Cole–Cole plot analysis in the IS, where both are frequency-dependent and can be used to determine the operational mechanisms in an OLED device, and can be simulated using a modeled equivalent circuit to ascertain the charge dynamics in individual organic layers at specific voltages, as shown in Fig. 20(c). Although the modulus Nyquist plot analysis is just the inverse of the complex impedance Nyquist plot analysis, its major advantage is the easy identification of multiple relaxation processes in complex materials with non-ideal dielectric behavior. Several groups have adopted this technique to analyze devices. For instance, Kim *et al.*[103] recently examined the relationship between efficiency and charge transport properties in green thermally activated delayed fluorescence (TADF) OLED devices using a complex modulus Cole–Cole plot. This technique was recently adopted by Chen's group[104] to estimate the charge dynamics in OLED devices with different charge-blocking layers with or without PDM characteristics. It was demonstrated that the modulus

Cole–Cole plot can exhibit different semicircles at different temperatures, which correspond to the organic layers/interfaces in the device at different voltages, owing to the charge injection, accumulation, and recombination dynamics occurring in the device.[105]

Another important form of IS is the *C–V* simulation to investigate the charge injection, accumulation, recombination, and SOP characteristics in molecules at different voltages. Kim *et al.*[106] leveraged this technique to investigate the minimization of polaron accumulation in the EML as an important physical factor for enhancing the lifetime and stability of OLED devices. The energy-level diagrams of the investigated devices are shown in Fig. 21(b). They simulated the *C–V* curves of the devices (Fig. 21(a)) to determine the charge distribution in each organic layer within the devices at different voltages to correlate the capacitance trend with the charge dynamics, as shown in Fig. 21(c) and (d). The group pointed out that charge accumulation at interfaces is caused by two major factors: the energy barrier and charge mobility. The exegeses of this observation were reported based on an investigation conducted to ascertain these phenomena in mixed- and single-host EML OLED devices. This observation asserts that an injected hole or electron of low mobility will be confined at the interfaces owing to its inability to overcome the energy barrier. Moreover, if a charge has approximately 1000 times higher mobility than an opposite charge, the rapid flow and accumulation of that charge at the interface will retard the flow of the opposite
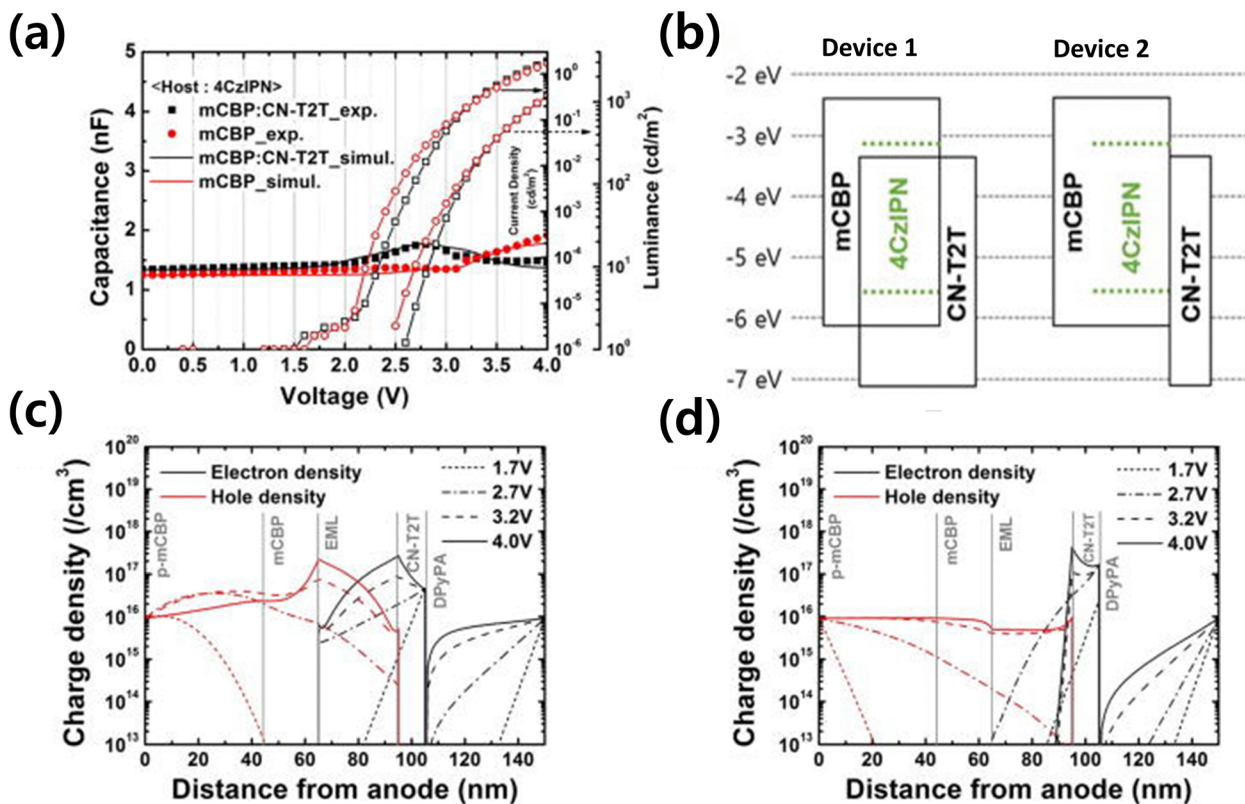
Fig. 21 (a) The capacitance–voltage characteristics of the OLEDs as a function of luminance and current density. (b) The energy-level diagrams of the mixed-host EML and single EML OLED devices. The distribution of the local charge densities of electrons and holes at different voltages in (c) mixed-host and (d) single-host–based OLEDs. Reproduced with permission from ref. 106 Copyright 2017, AIP Publishing.

charge, thereby lowering the mobility of the opposite charge to the adjacent layer. Other charge accumulation mechanisms, such as SOP, which were reported in the previous sections using IS, have also been confirmed using a C–V simulation technique.[107]

7. Synopsis and perspective

In this review, we discuss the major advances made by some pioneering groups as well as the recent advancements made in characterizing the operational mechanisms in OLED devices using impedance spectroscopy and equivalent circuit techniques. This technique provides an opportunity to rationalize the physical processes of various characteristic behaviors of OLED devices. In particular, IS and equivalent circuit simulations allow the investigation of the underlying mechanisms in each organic layer of OLED devices at different frequencies and time domains in terms of capacitive behavior, dielectric response, relaxation frequency, and conductivity, making it one of the best techniques for understanding the working mechanism of organic electronics.

In this regard, certain interesting features observed in the lower frequency range of a C–F curve can be simulated using a modeled equivalent circuit to extract information (resistance–capacitance values) on the trapping/detrapping processes, charge injection at the middle frequency, and geometric characteristics at high frequencies in each organic layer. These extracted parameter

values can also be used to generate information on other mechanisms, such as the density of state (DOS), charge activation energy, degradation mechanisms, and recombination as demonstrated. Not neglecting the fact that other curves like the Nyquist (Cole–Cole plot) and modulus plots can also be simulated using modeled equivalent circuits to acquire the aforementioned information on an OLED device. This technique has been made relatively easy through the developed user-friendly software with easy digital data processing to help novices better appreciate the technique, although some level of understanding is required.

Nonetheless, although this technique offers significant opportunities, pertinent improvements are required to fully explore the technique.

1. The resolution of the IS measurement must be increased to separate layers with similar relaxation times.

2. Measurements without noise, especially at low frequencies, using a Faraday cage, etc.

3. Modeling equivalent circuits with developed circuit elements that can imitate real situations in OLED devices.

4. Developing artificial intelligence (AI)-based smart simulations with optimized equivalent circuits.

5. The constant resistor must be replaced with an exponential resistor to ensure the in situ characterization of the experimental results.

These investigations from pioneering groups using IS and equivalent circuit simulations have provided a clear

understanding of the operational mechanisms and the effects of SOP and degradation in OLED devices, which intuitively demonstrates that IS and equivalent circuit simulations can be effectively employed in real industrial fields to investigate and enhance the performance of OLED devices.

Conflicts of interest

The authors declare no conflicts to declare.

Data availability

The authors confirm that all the data generated or analyzed during this study are included in the published review.

Acknowledgements

References

1 Y. Du, C. Li, R. Xu, L. Meng and Y. Bai, *ACS Appl. Mater. Interfaces*, 2025, **17**(4), 5578–5594, DOI: **10.1021/acsami. 4c11678**.

2 C. W. Tang, S. A. VanSlyke and C. H. Chen, *J. Appl. Phys.*, 1989, **65**(9), 3610, DOI: **10.1063/1.343409**.

3 S. A. Van Slyke, C. H. Chen and C. W. Tang, *Appl. Phys. Lett.*, 1996, **69**(15), 2160, DOI: **10.1063/1.117151**.

4 A. C. Brannan, H. H. Cho, A. P. M. Reponen, M. Linnolahti, M. Bochmann, N. C. Greenham and A. S. Romanov, *Adv. Mater.*, 2024, **36**(5), 2306249, DOI: **10.1002/adma.202306249**.

5 M. M. Raikwar, S. C. Kim, J. Sun, C. Chu and J. Y. Lee, *ACS Appl. Mater. Interfaces*, 2023, **15**(34), 40809, DOI: **10.1021/ acsami.3c08099**.

6 B. Qu, H. Zhao and S. R. Forrest, *ACS Photonics*, 2023, **10**(9), 3042, DOI: **10.1021/acsphotonics.3c00271**.

7 C. Wu, K. Shi, S. Li, J. Yan, Z. Q. Feng, K. N. Tong, S. W. Zhang, Y. Zhang, D. Zhang, L. S. Liao and Y. Chi, *EnergyChem*, 2024, 100120, DOI: **10.1016/j.enchem.2024.100120**.

8 Y. Wang, T. Yang, S. Dong, S. Zhao, W. Dong, H. Xu, X. Wang, Y. Miao and H. Wang, *ACS Mater. Lett.*, 2024, **6**(3), 1020–1028, DOI: **10.1016/j.enchem.2024.100120**.

9 M. Montrone, A. Maggiore, A. Moliterni, P. Pander, M. Pugliese, A. L. Capodilupo, S. Gambino, C. T. Prontera, V. Valenzano, F. Mariano and G. Accorsi, *J. Mater. Chem. C*, 2025, **13**(1), DOI: **10.1039/D4TC03239J**.

10 H. Wang, J. X. Chen, Y. Z. Shi, X. Zhang, L. Zhou, X. Y. Hao, J. Yu, K. Wang and X. H. Zhang, *Adv. Mater.*, 2024, **36**(8), 2307725, DOI: **10.1002/adma.202307725**.

11 Y. T. Lee, C. Y. Chan, N. Matsuno, S. Uemura, S. Oda, M. Kondo, R. W. Weerasinghe, Y. Hu, G. N. I. Lestanto,

Y. Tsuchiya and Y. Li, *Nat. Commun.*, 2024, **15**(1), 3174, DOI: **10.1038/s41467-024-47482-3**.

12 H. Sun, X. Zhang, S. Wang, D. Wang and C. Lee, *Org. Electron.*, 2024, **125**, 106985, DOI: **10.1016/j.orgel.2023.106985**.

13 L. Jäger, T. D. Schmidt and W. Brütting, *AIP Adv.*, 2016, **6**(9), DOI: **10.1063/1.4963796**.

14 N. Yoshida, H. Sasabe, H. Arai, Y. Sagae, Y. Yagi, K. Hoshi, D. Yokoyama and J. Kido, *Adv. Opt. Mater.*, 2024, **12**(11), 2302382, DOI: **10.1002/adom.202302382**.

15 X. Wu, X. Zhu, L. Sun, S. Zhang, Y. Ren, Z. Wang, X. Zhang, F. Yang, H. L. Zhang and W. Hu, *Chem. Soc. Rev*, 2025, **54**, 1699–1732, DOI: **10.1039/d4cs00987h**.

16 S. Ishihara, H. Hase, T. Okachi and H. Naito, *Org. Electron.*, 2011, **12**(8), 1364, DOI: **10.1016/j.orgel.2011.05.004**.

17 S. Berleb and W. Brütting, *Phys. Rev. Lett.*, 2002, **89**(28), 286601, DOI: **10.1103/PhysRevLett.89.286601**.

18 S. Liu, M. Guan, Y. Zhang, Y. Li, X. Liu, W. Sun, C. Liu and Y. Zeng, *Opt. Commun.*, 2018, **419**, 13, DOI: **10.1016/ j.optcom.2018.02.049**.

19 L. Niu, M. Guan, X. Chu, Y. Zeng, Y. Li and Y. Zhang, *J. Phys. Chem. C*, 2015, **119**(19), 10526, DOI: **10.1021/ acs.jpcc.5b03175**.

20 I. R. de Moraes, S. Scholz, B. Lüssem and K. Leo, *Org. Electron.*, 2011, **12**(2), 341, DOI: **10.1016/j.orgel.2010.11.004**.

21 S. Scholz, K. Walzer and K. Leo, *Adv. Funct. Mater.*, 2008, **18**(17), 2541, DOI: **10.1002/adfm.200700816**.

22 A. Gasonoo, J. M. Kim, S. J. Yoo, Y. J. Cho, J. H. Lee, Y. Choi, J. J. Kim and J. H. Lee, *Org. Electron.*, 2019, **67**, 242, DOI: **10.1016/j.orgel.2019.01.019**.

23 D. Son, K. Marumoto, T. Kizuka and Y. Shimoi, *Synth. Met.*, 2012, **162**(24), 2451, DOI: **10.1016/j.synthmet.2012.11.009**.

24 S. Väth, K. Tvingstedt, M. Auth, A. Sperlich, A. Dabulienė, J. V. Gražulevičius, P. Stakhira, V. Cherpak and V. Dyakonov, *Adv. Opt. Mater.*, 2017, **5**(3), 1–5, DOI: **10.1002/adom.201600926**.

25 T. Ogiwara, Y. Wakikawa and T. Ikoma, *J. Phys. Chem. A*, 2015, **119**(14), 3415, DOI: **10.1021/acs.jpca.5b02253**.

26 R. Walia, X. Xiong, X. C. Fan, T. F. Chen, H. Wang, K. Wang, Y. Z. Shi, X. Tang, J. L. Bredas, C. Adachi and X. K. Chen, *Nat. Mater.*, 2025, DOI: **10.1038/s41563-025-02309-4**.

27 K. Goushi, K. Yoshida, K. Sato and C. Adachi, *Nat. Photonics*, 2012, **6**(4), 253, DOI: **10.1038/nphoton.2012.31**.

28 X. Guo, P. Yuan, J. Fan, X. Qiao, D. Yang, Y. Dai, Q. Sun, A. Qin, B. Z. Tang and D. Ma, *Adv. Mater.*, 2021, **33**(11), 2006953, DOI: **10.1002/adma.202006953**.

29 X. Wu, S. Ni, C. H. Wang, W. Zhu and P. T. Chou, *Chem. Rev.*, 2025, **125**, 6685, DOI: **10.1021/acs.chemrev.5c00021**.

30 A. Endo, M. Ogasawara, A. Takahashi, D. Yokoyama, Y. Kato and C. Adachi, *Adv. Mater.*, 2009, **21**(47), 4802, DOI: **10.1002/adma.200900983**.

31 S. P. Kersten, A. J. Schellekens, B. Koopmans and P. A. Bobbert, *Phys. Rev. Lett.*, 2011, **106**(19), 197402, DOI: **10.1103/PhysRevLett.106.197402**.

32 S. Ishihara, H. Hase, T. Okachi and H. Naito, *J. Appl. Phys.*, 2011, **110**(3), DOI: **10.1063/1.3615950**.

33 T. Okachi, T. Nagase, T. Kobayashi and H. Naito, *Thin Solid Films*, 2008, **517**(4), 1331, DOI: **10.1016/j.tsf.2008.09.020**.

34 M. Mizusaki, *Mol. Cryst. Liq. Cryst.*, 2023, **766**(1), 51, DOI: **10.1080/15421406.2023.2220598**.

35 T. Yasuda and K. Sakamoto, *Jpn. J. Appl. Phys.*, 2024, DOI: **10.35848/1347-4065/ad8240**.

36 Y. Wu, J. Luo, C. Lin, T. Zhu, X. Qiao, D. Yang, Y. Dai, Q. Sun, J. Chen and D. Ma, *Phys. Chem. Chem. Phys.*, 2023, **25**(6), 4598, DOI: **10.1039/D2CP05797B**.

37 S. J. Kim, A. Raji, A. Gasonoo, J. Lee and J. H. Lee, *Org. Electron.*, 2023, **120**, 106850, DOI: **10.1016/j.orgel.2023.106850**.

38 C. S. Sangeeth, A. Wan and C. A. Nijhuis, *J. Am. Chem. Soc.*, 2014, **136**(31), 11134, DOI: **10.1021/ja505420c**.

39 U. Ahmadu, S. Tomas, S. A. Jonah, A. O. Musa and N. Rabiu, *Adv. Mater. Lett.*, 2013, **4**, 185–195, DOI: **10.5185/amlett.2012.7396**.

40 A. C. Lazanas and M. I. Prodromidis, *ACS Meas. Sci. Au*, 2023, **3**(3), 162, DOI: **10.1021/acsmeasuresciau.2c00070**.

41 P. Jash, R. K. Parashar, C. Fontanesi and P. C. Mondal, *Adv. Funct. Mater.*, 2022, **32**(10), 2109956, DOI: **10.1002/adfm.202109956**.

42 J. R. Macdonald, W. B. Johnson, I. D. Raistrick, D. R. Franceschetti, N. Wagner, M. C. H. McKubre, D. D. Macdonald, B. Sayers, N. Bonanos, B. C. H. Steele and E. P. Butler, *Impedance Spectroscopy: Theory, Experiment, and Applications*, John Wiley & Sons, 3rd edn, 2018, vol. 424. **https://elib.dlr.de/121440/**.

43 M. E. Orazem and B. Tribollet, *ECS Interface*, 2008, **1**(906), 383, DOI: **10.1002/9780470381588**.

44 A. Lasia, *Electrochemical Impedance Spectroscopy and its Applications*, Springer, MA, US, MAOE, Springer, 2002, vol. 32, DOI: **10.1007/0-306-46916-2_2**.

45 V. F. Lvovich, WLY, 2012. ISBN: 978-0-470-62778-5.

46 W. P. Gomes and D. Vanmaekelbergh, *Electrochim. Acta*, 1996, **41**(7), 967, DOI: **10.1016/0013-4686(95)00427-0**.

47 H. Shin, M. Yamamoto, M. Ha, S. S. Bae and C. Chu, *Symp. Dig. Tech. Pap.*, 2024, **21**(55), 256, DOI: **10.1002/sdtp.17503**.

48 C. K. Moon and M. C. Gather, *Adv. Opt. Mater.*, 2024, **2401253**, DOI: **10.1002/adom.202401253**.

49 B. Hirschorn, M. E. Orazem, B. Tribollet, V. Vivier, I. Frateur and M. Musiani, *Electrochim. Acta*, 2010, **55**(21), DOI: **10.1016/j.electacta.2009.10.065**.

50 P. Casolaro, V. Izzo, G. Giusi, N. Wyrsch and A. Aloisio, *J. Appl. Phys.*, 2024, **136**(11), DOI: **10.1063/5.0230008**.

51 G. J. Brug, A. L. Van den Eeden, M. Sluyters-Rehbach and J. H. Sluyters, *J. Electroanal. Chem. Interfacial Electrochem.*, 1984, **176**(1), DOI: **10.1016/S0022-0728(84)80324-1**.

52 S. Nowy, W. Ren, J. Wagner, J. A. Weber and W. Brütting, *Organic Light Emitting Materials and Devices XIII*, 2009, SPIE, vol. 7415, p. 79, DOI: **10.1117/12.824856**.

53 J. S. Kim, S. H. Kwon and Y. S. Kim, *Nanoscale*, 2023, **15**(4), 1529, DOI: **10.1039/D2NR05261J**.

54 H. Lee and T. Kim, *ACS Appl. Mater. Interfaces*, 2024, DOI: **10.1021/acsami.4c05175**.

55 J. M. Kim, K. H. Lee and J. Y. Lee, *Adv. Mater.*, 2023, **35**(14), 2209953, DOI: **10.1002/adma.202209953**.

56 H. D. Lee, H. J. Jang, J. H. Baek, J. J. Kim, H. C. Choi, J. M. Kim and J. Y. Lee, *Adv. Opt. Mater.*, 2023, **11**(2), DOI: **10.1002/adom.202202109**.

57 K. H. Lee, J. M. Kim and J. Y. Lee, *Adv. Opt. Mater.*, 2024, **12**(2), 2301358, DOI: **10.1002/adom.202301358**.

58 J. Jiang, H. J. Jang, K. H. Lee, J. Lim, J. M. Kim, S. Zhao and J. Y. Lee, *Adv. Opt. Mater.*, 2024, **12**(3), 2301484, DOI: **10.1002/adom.202301484**.

59 R. A. K. Yadav, D. K. Dubey, S. Z. Chen, T. W. Liang and J. H. Jou, *Sci. Rep.*, 2020, **10**(1), 9915, DOI: **10.1038/s41598-020-66946-2**.

60 T. Sasaki, T. Oono, T. Shimizu and H. Fukagawa, *Adv. Mater. Interfaces*, 2023, **10**(19), 2201925, DOI: **10.1002/admi.202201925**.

61 J. H. Lee, P. S. Wang, H. D. Park, C. I. Wu and J. J. Kim, *Org. Electron.*, 2011, **12**(11), 1763, DOI: **10.1016/j.orgel.2011.07.015**.

62 Y. Z. Shi, K. Wang, S. L. Zhang, X. C. Fan, Y. Tsuchiya, Y. T. Lee, G. L. Dai, J. X. Chen, C. J. Zheng, S. Y. Xiong and X. M. Ou, *Angew. Chem.*, 2021, **133**(49), 26082, DOI: **10.1002/ange.202108943**.

63 X. Zhou, J. Blochwitz, M. Pfeiffer, A. Nollau, T. Fritz and K. Leo, *Adv. Funct. Mater.*, 2001, **11**(4), 310, DOI: **10.1002/1616-3028(200108)11:4<310::AID-ADFM310>3.0.CO;2-D**.

64 D. Yokoyama, Y. Setoguchi, A. Sakaguchi, M. Suzuki and C. Adachi, *Adv. Funct. Mater.*, 2010, **20**(3), 386, DOI: **10.1002/adfm.200901684**.

65 Y. Noguchi, Y. Miyazaki, Y. Tanaka, N. Sato, Y. Nakayama, T. D. Schmidt, W. Brütting and H. Ishii, *J. Appl. Phys.*, 2012, **111**(11), DOI: **10.1063/1.4724349**.

66 S. Altazin, S. Züfle, E. Knapp, C. Kirsch, T. D. Schmidt, L. Jäger, Y. Noguchi, W. Brütting and B. Ruhstaller, *Org. Electron.*, 2016, **39**, 244, DOI: **10.1016/j.orgel.2016.10.014**.

67 F. Tenopala-Carmona, D. Hertel, S. Hillebrandt, A. Mischok, A. Graf, P. Weitkamp, K. Meerholz and M. C. Gather, *Nat. Commun.*, 2023, **14**(1), 6126, DOI: **10.1038/s41467-023-41841-2**.

68 Y. Noguchi, Y. Tanaka, H. Ishii and W. Brütting, *Synth. Met.*, 2022, **288**, 117101, DOI: **10.1016/j.synthmet.2022.117101**.

69 M. Weis, T. Otsuka, D. Taguchi, T. Manaka and M. Iwamoto, *J. Appl. Phys.*, 2015, **117**(15), DOI: **10.1063/1.4918556**.

70 R. Warren, P. W. Blom and N. Koch, *Appl. Phys. Lett.*, 2023, **122**(15), DOI: **10.1063/5.0146194**.

71 T. Okachi, T. Nagase, T. Kobayashi and H. Naito, *Thin Solid Films*, 2008, **517**(4), 1327, DOI: **10.1016/j.tsf.2008.09.019**.

72 C. C. Chen, B. C. Huang, M. S. Lin, Y. J. Lu, T. Y. Cho, C. H. Chang, K. C. Tien, S. H. Liu, T. H. Ke and C. C. Wu, *Org. Electron.*, 2010, **11**(12), 1901, DOI: **10.1016/j.orgel.2010.09.005**.

73 J. Drechsel, M. Pfeiffer, X. Zhou, A. Nollau and K. Leo, *Synth. Met.*, 2002, **127**(1), 201, DOI: **10.1016/S0379-6779(01)00623-3**.

74 S. Züfle, S. Altazin, A. Hofmann, L. Jäger, M. T. Neukom, W. Brütting and B. Ruhstaller, *J. Appl. Phys.*, 2017, **122**(11), DOI: **10.1063/1.4992041**.

75 S. Nowy, W. Ren, A. Elschner, W. Lövenich and W. Brütting, *J. Appl. Phys.*, 2010, **107**(5), DOI: **10.1063/1.3294642**.

76 P. Chulkin, O. Vybornyi, M. Lapkowski, P. J. Skabara and P. Data, *J. Mater. Chem. C*, 2018, **6**(5), 1008, DOI: **10.1039/C7TC04599A**.

77 B. Ray, A. G. Baradwaj, B. W. Boudouris and M. A. Alam, *J. Phys. Chem. C*, 2014, **118**(31), 17461, DOI: **10.1021/jp505500r**.

78 L. Burtone, J. Fischer, K. Leo and M. Riede, *Phys. Rev. B: Condens. Matter Mater. Phys.*, 2013, **87**(4), 045432, DOI: **10.1103/PhysRevB.87.045432**.

79 P. Pahner, H. Kleemann, L. Burtone, M. L. Tietze, J. Fischer, K. Leo and B. Lüssem, *Phys. Rev. B: Condens. Matter Mater. Phys.*, 2013, **88**(19), 195205, DOI: **10.1103/PhysRevB.88.195205**.

80 L. Burtone, D. Ray, K. Leo and M. Riede, *J. Appl. Phys.*, 2012, **111**(6), DOI: **10.1063/1.3693545**.

81 H. Hatta, Y. Miyagawa, T. Nagase, T. Kobayashi, T. Hamada, S. Murakami, K. Matsukawa and H. Naito, *Appl. Sci.*, 2018, **8**(9), 1493, DOI: **10.3390/app8091493**.

82 H. Lee, K. J. Kim, Y. J. Moon, Y. K. Kim and T. Kim, *Org. Electron.*, 2020, **84**, 105816, DOI: **10.1016/j.orgel.2020.105816.**

83 J. H. Park, Y. J. Shin, I. Kymissis, Y. Jeon and C. H. Kim, *J. Mater. Chem. C*, 2023, **11**(28), 9670, DOI: **10.1039/D3TC01171B**.

84 N. Ahn, K. Kwak, M. S. Jang, H. Yoon, B. Y. Lee, J. K. Lee, P. V. Pikhitsa, J. Byun and M. Choi, *Nat. Commun.*, 2016, **7**(1), 13422, DOI: **10.1038/ncomms13422**.

85 T. D. Schmidt, L. Jäger, Y. Noguchi, H. Ishii and W. Brütting, *J. Appl. Phys*, 2015, **117**(21), DOI: **10.1063/1.4921829**.

86 T. Okachi, T. Nagase, T. Kobayashi and H. Naito, *Jpn. J. Appl. Phys.*, 2008, **47**(12R), 8965, DOI: **10.1143/JJAP.47.8965**.

87 C. Weichsel, L. Burtone, S. Reineke, S. I. Hintschich, M. C. Gather, K. Leo and B. Lüssem, *Phys. Rev. B: Condens. Matter Mater. Phys.*, 2012, **86**(7), 075204, DOI: **10.1103/PhysRevB.86.075204**.

88 A. Gasonoo, Y. J. Lim, E. J. Jang, J. Lee, M. H. Kim, Y. Choi and J. H. Lee, *Mater. Today. Energy*, 2021, **21**, 100794, DOI: **10.1016/j.mtener.2021.100794**.

89 S. Y. Boo, A. Raji, J. Y. Park, S. Park, J. Lee and J. H. Lee, *J. Inf. Disp.*, 2024, **25**(2), 211, DOI: **10.1080/15980316.2023.2271176**.

90 Y. Noguchi, H. J. Kim, R. Ishino, K. Goushi, C. Adachi, Y. Nakayama and H. Ishii, *Org. Electron.*, 2015, **17**, 184, DOI: **10.1016/j.orgel.2014.12.009**.

91 J. H. Lee and M. H. Kim, *Org. Electron.*, 2016, **28**, 172, DOI: **10.1016/j.orgel.2015.10.034**.

92 H. K. Choi, S. H. Lee, Y. J. Lim, S. T. Lee, J. H. Lee and J. H. Lee, *AIP Adv.*, 2020, **10**(6), DOI: **10.1063/5.0011699**.

93 A. Al Haddad, A. Picot, L. Canale, P. Dupuis, G. Zissis and P. Maussion, *IEEE Trans. Ind. Appl.*, 2021, **58**(1), 996, DOI: **10.1109/TIA.2021.3123096**.

94 I. H. Park, S. E. Lee, Y. Kim, S. Y. You, Y. K. Kim and G. T. Kim, *Org. Electron.*, 2022, **101**, 106404, DOI: **10.1016/j.orgel.2021.106404**.

95 J. Jiang, S. Zhao and J. Y. Lee, *Symp. Dig. Tech. Pap.*, 2024, **55**, 405, DOI: **10.1002/sdtp.17094**.

96 T. D. Schmidt, L. Jäger, Y. Noguchi, H. Ishii and W. Brütting, *J. Appl. Phys.*, 2015, **117**(21), DOI: **10.1063/1.4921829**.

97 G. W. Lee, H. Kim, J. Park, J. I. Shim and D. S. Shin, *IEEE Photonics Technol. Lett.*, 2018, **30**(13), 1183, DOI: **10.1109/LPT.2018.2838099**.

98 D. H. Kim, J. H. Hwang, E. Seo, K. Lee, J. Lim and D. Lee, *ACS Appl. Mater. Interfaces*, 2024, DOI: **10.1021/acsami.4c07049**.

99 T. Okachi, T. Nagase, T. Kobayashi and H. Naito, *Appl. Phys. Lett.*, 2009, **94**(4), DOI: **10.1063/1.3073043**.

100 K. Takagi, T. Nagase, T. Kobayashi and H. Naito, *Appl. Phys. Lett.*, 2016, **108**(5), DOI: **10.1063/1.4941235**.

101 M. Takada, T. Mayumi, T. Nagase, T. Kobayashi and H. Naito, *Appl. Phys. Lett.*, 2019, **114**(12), DOI: **10.1063/1.5066605**.

102 C. Kok, C. Doyranli, B. Canımkurbey, S. P. Mucur and S. Koyuncu, *RSC Adv.*, 2020, **10**(32), 18639, DOI: **10.1039/D0RA02527E**.

103 H. Lee, K. J. Kim, Y. J. Moon, Y. K. Kim and T. Kim, *Org. Electron.*, 2020, **84**, 105816, DOI: **10.1016/j.orgel.2020.105816**.

104 J. Nan, Y. Zhang, Z. Huang, L. Chen and B. G. Lee, *Symp. Dig. Tech. Pap.*, 2024, **55**, 260, DOI: **10.1002/sdtp.17504**.

105 J. Scherbel, P. H. Nguyen, G. Paasch, W. Brütting and M. Schwoerer, *J. Appl. Phys.*, 1998, **83**(10), 5045, DOI: **10.1063/1.367321**.

106 J. M. Kim, C. H. Lee and J. J. Kim, *Appl. Phys. Lett.*, 2017, **111**(20), DOI: **10.1063/1.5004623**.

107 R. Häusermann, S. Jenatsch, J. Leganés Carballo, H. Sharifidehsari, B. Blülle, S. Züfle, G. Liaptsis and B. Ruhstaller, *Symp. Dig. Tech. Pap.*, 2021, **52**, 341, DOI: **10.1002/sdtp.14686**.